Supplementary Information for

Microsecond and millisecond dynamics in the photosynthetic protein LHCSR1 observed by single-molecule correlation spectroscopy

Toru Kondo[a,*], Jesse B. Gordon[a], Alberta Pinnola[b], Luca Dall'Osto[b], Roberto Bassi[b,c], and Gabriela S. Schlau-Cohen[a,†]

[a] *Department of Chemistry, Massachusetts Institute of Technology,* [b] *Department of Biotechnology, University of Verona* [c] *Istituto per la Protezione delle Piante (IPP), Consiglio Nazionale delle Ricerche (CNR)*

(Dated: April 5, 2019)

* tkondo@mit.edu

† gssc@mit.edu

www.pnas.org/cgi/doi/10.1073/pnas.1821207116

CONTENTS

SUPPLEMENTARY INFORMATION

1. Fluorescence lifetime distribution analysis using 1D-ILT

The fluorescence decay profile, $F(t)$ (Fig. S1*A*, red), was constructed by calculating a histogram of the photon arrived time t, which is the emission time. The model function for the fluorescence decay, $F^s(t)$, is given by

$$F^s(t) = \sum_{k=1}^{L} a(\tau_k) F^{exp}(t, \tau_k), \quad [1]$$

where $a(\tau_k)$ is the amplitude of exponential decay component k with the lifetime of τ_k, corresponding to the fluorescence lifetime distribution, and L is the total number of the decay component. The exponential decay function, $F^{exp}(t, \tau_k)$, is given by convolution with an experimentally-measured instrument response function, IRF(t) (Fig. S1*A*, black):

$$F^{exp}(t, \tau) = \sum_{i=1}^{P} \mathrm{IRF}(t_i - t_0) \exp(-\frac{t - t_i}{\tau}), \quad [2]$$

where t_0 is a time offset for the IRF(t), and P is a total number of data points along t. The $a(\tau)$ can be derived by the one-dimensional inverse Laplace transformation (1D-ILT) of the $F^s(t)$. To stably perform the 1D-ILT, the experimental decay $F(t)$ was fitted with the maximum entropy method (MEM). In the MEM, the fitting was repeated to minimize the factor Q, given by Ref. (1)

$$Q = \chi^2 - \frac{2S}{\eta}. \quad [3]$$

χ^2 is the chi-square described by

$$\chi^2 = \frac{1}{P} \sum_{i=1}^{P} \frac{(F(t_i) - F^s(t_i))^2}{F(t_i) + F_0}, \quad [4]$$

where F_0 is a mean value of $F(t)$, used as an offset. S indicates the entropy relative to a model m corresponding to a prior distribution as given by

$$S = \sum_{k=1}^{L} \left\{ a(\tau_k) - m - a(\tau_k) \ln \frac{a(\tau_k)}{m} \right\}. \quad [5]$$

In the present study, m was represented as a flat distribution:

$$m = \frac{1}{L} \sum_{k=1}^{L} a(\tau_k). \quad [6]$$

The constant η regulates the ratio of S in the factor Q. Initially, η is set to a small value, so that S is dominant in Q. In this case, the distribution is biased to the model distribution m, avoiding the fitting being trapped in a local minimum. By increasing η, the fitting curve gradually converges to the experimental decay curve, and eventually the lifetime distribution $a(\tau_k)$ can be estimated. The fitting result of $a(\tau_k)$ was somewhat unstable and sensitive to the time offset t_0 of the IRF(t) as shown in Fig. S1*B*. Therefore, distributions calculated with thirteen different values for t_0s (Fig. S1*D*), each exhibiting a low χ^2 for the fitting, were averaged to obtain a reasonable result, as shown in Fig. S1*C*.

2. 2D-FLC analysis using 2D-ILT

The purpose of the analysis is to estimate the two-dimensional fluorescence lifetime correlation (2D-FLC) composed of two functions; the fluorescence lifetime distribution, A, and the correlation function, G. First, we constructed the two-dimensional fluorescence decay (2D-FD) matrix, M. Then, the 2D-FLC matrix, $\tilde{M}$, was calculated by the two-dimensional inverse Laplace transformation (2D-ILT) of M using the fitting analysis with MEM. The procedure of 2D-FLC analysis is described in the following sections (see also Ref. (1–3) for details). The stability of the analysis algorithm was confirmed with an artificial photon stream generated by Monte Carlo simulation as shown in Fig. S2.

2-1. Photon stream generated by Monte Carlo simulation

Photon data was simulated for a simple two-state system, characterized by the fluorescence intensity and lifetime of each state and the rate matrix of transition between them. Fig. S2*A* displays the simulation parameters, where an element of the rate matrix, K_{ji}, corresponds to a transition rate from state i to j at $i \neq j$ as well as a rate of the molecule being lost at $i = j$ (e.g. due to the photobleaching or molecular diffusion). The measurement (T) and emission time (t), which is the photon detection time with respect to the measurement start time and each pulse excitation, respectively, were given for each photon based on a stochastic calculation according to the intensity and lifetime, respectively. The experimentally-obtained IRF(t) of our setup was used in the calculation of t. At time intervals of 10^{-6} s, we checked whether the transition event occurred or not based on the transition probability calculated from the rate matrix. Repeating the routine $\sim 10^9$ times produced a photon stream composed of enough data sets of T and t for the 2D-FLC analysis, which is displayed as a time trace of photon number in Fig. S2*B*.

2-2. Construction of 2D-FD map $M(\Delta T, t', t'')$

Fig. S2*C* shows an illustration of a photon stream used to construct the 2D-FD map. Photon pairs separated by a time interval of ΔT are found in the stream data, and all photons within the time window ($\Delta\Delta T$) are counted. The emission times (t', t'') of each photon in the pair is taken such that each pair provides one data point on the $t' - t''$ 2D distribution map. By constructing a 2D histogram of (t', t'') for all photon pairs, we can obtain the 2D-FD map at each ΔT, i.e. a P-by-P matrix $M(\Delta T, t', t'')$, as in Fig. S2*D*. The 2D data, which should be symmetric with respect to the exchange between t' and t'' if the system is in the equilibrium state, usually includes asymmetric backgrounds due to the experimental noise. To eliminate the background, $M(\Delta T, t', t'')$ and $M(\Delta T, t'', t')$ were averaged. The 2D-FD maps calculated at different ΔTs exhibit distinct decay profiles, indicating time changes in the fluorescence correlation.

2-3. Transformation of 2D-FD matrix $M(\Delta T, t', t'')$ into 2D-FLC matrix $\tilde{M}(\Delta T, \tau', \tau'')$ to derive correlation function $G(\Delta T)$

Here, we describe the 2D-ILT of $M(\Delta T, t', t'')$ into $\tilde{M}(\Delta T, \tau', \tau'')$ in matrix form, i.e. transformation of a matrix related to the fluorescence decay time t into that related to the fluorescence lifetime τ. $\tilde{M}(\Delta T)$, a L-by-L matrix in τ-space, is associated with $M(\Delta T)$, a P-by-P matrix in t-space, as below:

$$M(\Delta T) = D \cdot \tilde{M}(\Delta T) \cdot D^{\mathrm{T}}, \qquad [7]$$

where D, a P-by-L matrix storing exponential decay functions with various lifetimes in the range from τ_1 to τ_L, is given by,

$$D = \begin{pmatrix} F^{exp}(t_1, \tau_1) & \dots & F^{exp}(t_1, \tau_L) \\ \vdots & \ddots & \vdots \\ F^{exp}(t_P, \tau_1) & \dots & F^{exp}(t_P, \tau_L) \end{pmatrix}. \qquad [8]$$

The $F^{exp}(t, \tau)$ indicates an exponential function convoluted with the IRF(t) according to Eq. [2]. Then, the 2D-FLC matrix $\tilde{M}(\Delta T)$ is represented as

$$\tilde{M}(\Delta T) = A \cdot G(\Delta T) \cdot A^{\mathrm{T}}. \qquad [9]$$

A is a L-by-N matrix independent of ΔT, corresponding to the τ distribution. Here, N indicates a total number of states, each of which exhibits a distinct τ distribution. $G(\Delta T)$ is a N-by-N symmetric matrix, corresponding to the correlation function at ΔT. Thus, $M(\Delta T)$ can be reproduced by calculating $D \cdot A \cdot G(\Delta T) \cdot A^{\mathrm{T}} \cdot D^{\mathrm{T}}$, where $G(\Delta T)$ and A are unknown while D can be pre-calculated. We calculated a model 2D-FD matrix, $M^s(\Delta T)$, by fitting the experimentally-obtained $M(\Delta T)$ using 2D-MEM with variable matrices of $G(\Delta T)$ and A. The 2D-MEM is essentially the same as 1D-MEM described in the section 1. Hence, the fitting was repeated to minimize the factor Q in Eq. [3], where the chi-square χ^2 and entropy S are extended to two dimensions:

$$\chi^2 = \frac{1}{P^2} \sum_{i=1}^{P} \sum_{j=1}^{P} \frac{(M_{ji} - M_{ji}^s)^2}{M_{ji} + M_0} \quad [10]$$

$$S = \sum_{n=1}^{N} \sum_{k=1}^{L} \left\{ a_n(\tau_k) - m_n - a_n(\tau_k) \ln \frac{a_n(\tau_k)}{m_n} \right\} \quad [11]$$

$$m_n = \frac{1}{L} \sum_{k=1}^{L} a_n(\tau_k). \quad [12]$$

where $M_{ji}^{(s)}$ is an element of $M^{(s)}(\Delta T)$, and M_0 is the mean value of $M(\Delta T)$ used as an offset. By increasing η in the factor Q, we can obtain a reasonable fitting result. In the actual analysis (see next paragraph), the matrices $M(\Delta T)$s at various ΔTs were globally fitted with a global variable of A, in which χ^2 is defined as a summation of that at each ΔT.

2-4. Procedure for 2D-FLC analysis

The 2D-FLC analysis was performed by the following steps. All analysis algorithms were built with MATLAB software (The MathWorks, Inc.).

Step 1: A total number of states, i.e. N, exhibiting distinct fluorescence lifetimes was preliminarily estimated from the lifetime distribution given by the 1D-ILT as described in section 1.

Step 2: The 2D-FD matrix, $M(\Delta T)$, was created at various ΔTs ranging from 10^{-4} to 10^{1} s as shown in Fig. S2*D* and the upper panels of Fig. S2*E*.

Step 3: The initial values of matrix A, hereafter A_0, were estimated from the 2D-MEM fitting of $M(\Delta T_{min})$, where ΔT_{min} is the shortest $\Delta T = 10^{-4}$ s.

Step 4: The correlation matrix $G(\Delta T)$ was estimated separately at various ΔTs with the constant A_0, and defined as $G_0(\Delta T)$.

Step 5: By inputting the A_0 and $G_0(\Delta T)$s as initial parameters, the global fitting of all $M(\Delta T)$s at various ΔTs was performed. In the fitting, the matrix A was treated as a global variable while the matrix $G(\Delta T)$ was treated as a local variable for each ΔT. Then, a reasonable model matrix $M^s(\Delta T)$, as shown in the lower panels of Fig. S2*E*, was estimated at each ΔT by minimizing the factor Q. As a result, we obtained A and $\tilde{M}(\Delta T)$ as shown in Fig. S2*F-H*. The correlation function $G(\Delta T)$ was also obtained based on Eq. [9].

Step 6: To fit the correlation function, as described in the next section, the $G(\Delta T)$ was normalized as:

$$\tilde{M}(\Delta T) = A \cdot G(\Delta T) \cdot A^{\mathrm{T}} = (A \cdot U^{-1}) \cdot (U \cdot G(\Delta T) \cdot U) \cdot (U^{-1} \cdot A^{\mathrm{T}}), \quad [13]$$

where U is a N-by-N diagonal matrix used to normalize A with respect to the total photon number in each state. Thus, the diagonal elements of U are given by

$$U_{nn} = \sum_{k=1}^{L} A_{kn} \tau_k, \quad [14]$$

where A_{kn} is an element of A, and τ_k corresponds to a photon number provided by the exponential decay component with a lifetime of τ_k, i.e. $\tau_k = \int_0^\infty \exp(-t/\tau_k) dt$. The normalization transfers all information about the fluorescence intensity to $U \cdot G(\Delta T) \cdot U$, assuring that the correlation analysis described in the following section is available for the estimation of not only the dynamics rate but also the fluorescence intensity. Hereafter, the normalized correlation function $U \cdot G(\Delta T) \cdot U$ is defined as $G^n(\Delta T)$. Thus, the 2D-FLC analysis finally provides the $G^n(\Delta T)$ as displayed in Fig. S2*I*

Step 7: When we analyzed the actual data, steps 1 to 6 were repeatedly executed at various t_0s for the IRF(t) given by Eq. [2] as shown in Fig. S1*E*. Then, five results exhibiting low chi-squares were averaged to avoid an anomalous fitting and make the obtained correlation clear. The averaged result was utilized in the following analysis of correlation function.

3. Fitting of correlation function $G^n(\Delta T)$

The normalized correlation function $G^n(\Delta T)$, estimated from the 2D-FLC analysis above, was fitted by a model function $G^s(\Delta T)$, which is a matrix composed of elements $G^s_{ji}(\Delta T)$ corresponding to auto-correlation when $j = i$ and cross-correlation when $j \neq i$. Based on Ref. (4), $G^s_{ji}(\Delta T)$ is given by

$$G^s_{ji}(\Delta T) = q^2 J^2 I \epsilon_j \epsilon_i \phi_j \phi_i c_i \times R_{ji}(\Delta T), \quad [15]$$

where q accounts for experimental factors such as the detection efficiency, filter transmittance, gain of the detector, etc., in our setup, I is the total photon number proportional to the total measurement time T^{total}, and J is the laser power. ϵ_j, ϕ_j, and c_i are the optical extinction coefficient, fluorescence quantum yield, and population of state j, respectively. $R_{ji}(\Delta T)$ is a matrix element derived from

$$R(\Delta T) = X \cdot \begin{pmatrix} \exp(\lambda_1 \Delta T) & 0 & \cdots \\ 0 & \exp(\lambda_2 \Delta T) & \\ \vdots & & \ddots \end{pmatrix} \cdot X^{-1}. \quad [16]$$

X is a matrix formed by eigenvectors corresponding to the eigenvalues λ. These are calculated by diagonalization of the rate matrix K defined by

$$\frac{\mathrm{d}}{\mathrm{d}\Delta T} P(\Delta T) = K \cdot P(\Delta T), \quad [17]$$

where $P(\Delta T)$ is a vector containing the population of each state at ΔT. By using the $R(\Delta T)$, c_i is calculated as

$$c_i = P_i(\infty) = \sum_j R_{ji}(\infty). \quad [18]$$

In the present study, q, J, and ϵ can be assumed to be constant irrespective of the state because of little spectral difference between the states. Therefore, the correlation function $G^n(\Delta T)$ is practically a function of I, ϕ, and K, so we can estimate the fluorescence intensity and dynamics rates from the global-fitting of the correlation curve that is an element of $G^n(\Delta T)$. The fine fitting as shown by black lines in Fig. S2*J* provides reasonable parameters for the fluorescence intensity and rate matrix as listed in Fig. S2*K*. Here, it is to be noted that the fluorescence intensity is not absolute but a relative value and thus required to be normalized by $\sqrt{I}$ or $\sqrt{T^{total}}$ for the comparison of photon streams taken in distinct samples with different measurement times (see the following section and Fig. S3*D*).

The Eq. [15] can be rewritten in the matrix form:

$$G^s(\Delta T) = q^2 J^2 I \cdot \Big[E \cdot \Phi \cdot R(\Delta T)\Big] \cdot \Big[E \cdot \Phi \cdot C\Big], \quad [19]$$

where E, Φ, and C indicate a diagonal matrix composed of ϵ_i, ϕ_i, and c_i, respectively. $G^s(\Delta T)$ reflects the correlation between the first and second photons, separated by a time interval of ΔT as illustrated in Fig. S2*C*. The contributions of the first and second photons are given by the terms, $E \cdot \Phi \cdot C$ and $E \cdot \Phi \cdot R(\Delta T)$, respectively. Here, it should be noted that Eq. [19] is applicable only for the case that the paired photons are radiated from the same emitter, i.e. all correlated states are connected to each other within one energy landscape. Thus, Eq. [19] suits systems including those where several dynamics take place sequentially. On the other hand, in the complicated system comprised of multiple independent emitters, the first and second photons could be radiated from different emitters. The second photon that is not correlated with the first one also contributes to the correlation function as an interference between independent components. Therefore, the interference contribution should be added in the term of $E \cdot \Phi \cdot R(\Delta T)$ in Eq. [19] as below (see also following sections):

$$G^s(\Delta T) = q^2 J^2 I \cdot \sum_x \left(\Big[\sum_{y \neq x} \big\{ E_y \cdot \Phi_y \cdot R_y(\infty) \big\} + E_x \cdot \Phi_x \cdot R_x(\Delta T) \Big] \cdot \Big[E_x \cdot \Phi_x \cdot C_x \Big] \right), \quad [20]$$

where x and y indicate the component number. The summation term for component y, corresponding to the interference between components, is irrelevant to ΔT, and thus contributes to $G^s(\Delta T)$ as a base correlation. The model correlation function $G^s(\Delta T)$ was utilized to fit $G^n(\Delta T)$ estimated by the 2D-FLC analysis.

4. Demonstration of 2D-FLC analysis using artificial photon streams

We confirmed the feasibility of 2D-FLC analysis by applying it to artificial photon streams that were simulated with the two-states model under various conditions (Fig. S3). Asymmetric and antisymmetric dynamics, in which the transition rate is different between forward and backward processes, were well fitted to provide reasonable parameters of the intensity and transition rates as in Fig. S3*A*, *B*, *F*, and *G*. Fig. S3*C* and *H* show that differences in the fluorescence intensity between the two states are distinguishable. If the total measurement time T was twice as in Fig. S3*D* and *I*, the intensity parameter increased up to 1.41 ($=\sqrt{2}$) times, suggesting a proportionality of $\sqrt{T}$. Therefore, the relative intensity can be estimated by normalizing with $\sqrt{T}$, even for distinct samples. In the case that the loss of target molecule happens at a rate given as a diagonal component of the rate matrix, the 2D-FLC analysis also provided reasonable results as shown in Fig. S3*E* and *J*. In actual experiments, the molecular loss can be induced by photobleaching and molecular diffusion. Thus, the 2D-FLC analysis is useful for a variety of dynamics.

5. Identification of multiple independent dynamics

The protein complex serving as the scaffold of the biological chromophore has many degrees of conformational freedom creating a complicated energy landscape consisting of many local minimums, each of which corresponds to a conformational substate. The transitions between the substates are generally described as stochastic processes. Because the random walk on the potential surface leads to whole substates, we are able to examine the energy landscape by a long time observation of a single protein as illustrated in Fig. S4*A*. The multiple dynamics, reflecting a Markov chain, can be represented by a rate matrix as stated in the upper panel of Fig. S4*C*. We simulated a photon stream for the two-state system, in which all states are connected through two dynamics components, i.e. two off-diagonal terms in the rate matrix. Then, the photon stream was analyzed by the 2D-FLC algorithm to estimate the correlation function shown in the lower panel of Fig. S4*C*. It should be noted that the cross-correlation between state 1 and 2 is zero at short ΔT, indicating no base correlation. Therefore, as shown in Fig. S4*E*, we can fit the correlation curves using Eq. [19].

On the other hand, multiple independent dynamics, which take place simultaneously but asynchronously, are widely found in chromoproteins containing many pigments as in Fig. S4*B*. The system represented by independent rate matrices causes a base correlation in the cross-correlation curve as shown in Fig. S4*D*. The base correlation is caused by the interference between the independent dynamic components. Therefore, the correlation curves cannot be fitted by Eq. [19] containing no interference contribution, even assuming two independent dynamics components (Fig. S4*F*, solid lines). To reproduce the base correlation, Eq. [20] incorporating the interference contribution is needed (Fig. S4*F*, dotted lines). The correlation analysis of the multiple independent dynamics provides reasonable results for the relative fluorescence intensity of each state as well as the rate matrix, identifying each dynamic component under various conditions (Fig. S5). Thus, the independent dynamics occurring in discrete sites in a single protein can be distinguishable from the base correlation, and the properties can be analyzed by the correlation fitting using Eq. [20]. Here, we emphasize that measurement of diffusing samples makes this aspect of the analysis impossible because the probability of simultaneous excitation of two or more protein complexes can not be removed even in dilute solution (2). Therefore, the observation of single immobilized protein complexes is more suited to analyze complicated multiple dynamics such as in the photosynthetic system containing a number of fluorescence emitters (Fig. S4*B*).

6. Contribution of background to the base correlation in cross-correlation

As discussed above, the base correlation in the cross-correlation curve is caused by multiple independent dynamics, and hence utilized as an indicator to distinguish between sequential and individual dynamics. Meanwhile, the non-correlated contribution could also come from the background signal, which is due to the fluorescence from the buffer, coverslip, optics in the setup, etc. as well as the dark noise of the detector. To check this contribution, we measured the background signal on a dark area in a fluorescence image. The background level was estimated to be ca. 150 cps, and a lifetime of ca. 0.15 ns was given by the 1D-ILT analysis as shown in Fig. S6*A*-*C*. Then, we simulated a photon stream with the two-states model including a non-dynamical component (BG) characterized by the background intensity and lifetime (Fig. S6*D*). The correlation function was estimated for various intensities of the dynamics component, i.e. various intensity ratios between the BG and dynamic components, using the 2D-FLC analysis (Fig. S6*E*). Fig. S6*F* shows an increase in the contribution of BG to the cross-correlation, suggesting the relative intensity of the base correlation to the correlation change in the cross-correlation curve to be almost proportional to the intensity of BG. Meanwhile, the contribution seems to saturate at higher intensity ratios, and is less than the base correlation caused by the interference contribution of multiple dynamics. Therefore, the contribution of BG to the base correlation in cross-correlation is negligible.

7. Calculation of free-energy difference

The present correlation analysis provides rate constants of protein dynamics between quenched (Q) and active (A) states. The dynamics rate is related to an activation energy as described in the Arrhenius equation:

$$k_{Q\to A} = A\exp(-\frac{E^*_{Q\to A}}{k_BT}), \quad [21]$$

$$k_{A\to Q} = A\exp(-\frac{E^*_{A\to Q}}{k_BT}), \quad [22]$$

where $k_{Q\to A}$ and $E^*_{Q\to A}$ ($k_{A\to Q}$ and $E^*_{A\to Q}$) are the rate constant and activation energy, respectively, for the transition from Q to A state (A to Q state). A is a constant called the frequency factor, K_B is the Boltzmann constant, and T is an absolute temperature. When equilibrated between Q and A states, the free-energy difference, ΔE^*, is given by

$$\frac{k_{Q\to A}}{k_{A\to Q}} = \exp(-\frac{\Delta E^*}{k_BT}). \quad [23]$$

$\Delta E^* = E^*_{Q\to A} - E^*_{A\to Q}$ is positive when $k_{Q\to A} < k_{A\to Q}$ (quenched-biased), while negative when $k_{Q\to A} > k_{A\to Q}$ (active-biased). From Eq. [23] with the experimentally-obtained dynamics rates and $T = 300$ K, we can calculate ΔE^*. The free-energy difference reflects an energetic difference between local potential minimums in the protein energy landscape as described in the center panel of Fig. 3*A*-*F*, where activation energies between Q and A states were tentatively calculated for scaling the potential barrier by assuming the constant A in Eq. [21] to be 1000. In that case, the activation energy for the dynamic component likely corresponding to the Lut1/Chl *a* pair in LHCB1-7.5 (Fig. 3*E*, blue) is calculated to be around 800 cm^{-1}, consistent with 500-700 cm^{-1} estimated experimentally in LHCII (5, 6). Thus, the novel correlation analysis in the present study, which can identify the multiple independent dynamics in a chromoprotein, allows estimation of the energetic properties of a binding site of a chromophore.

8. Standard deviations for the 2D-FLC and correlation fitting analyses

The accuracy of our analytical method was tested by bootstrapping the data as described below. First, we randomly picked complexes of LHCSR1-V-7.5, where it was allowed to choose the same complex up to twice until a total photon number reached to 3.3×10^7. We prepared five different data sets of photon stream from the randomly-grouped complexes. The 2D-FLC analysis was performed for each photon stream data to estimate the lifetime distribution and correlation curves as illustrated in Fig. S2, and then their standard deviations (± S.D.) were estimated as shown in Fig. S12. Averaged standard deviations of auto- and cross-correlation (1-1, 2-2, and 1-2) were calculated to be 4.7, 3.5, and 2.5%, respectively. Thus, the 2D-FLC analysis provides the correlation function with the deviation of less than 5%.

The deviations also cause variations in the dynamic properties estimated by the correlation fitting analysis as shown in Fig. S13. The standard deviation of the dynamic properties are summarized in Table S2. The fluorescence intensity and lifetime of the dynamic components, i.e. red and blue components, exhibit deviations of 11.3 and 2.2%, respectively, on average. Averaged standard deviation of the dynamics rate is 25.3%, leading to deviations of 16.1% in the free-energy difference as well as 8.0% in the state population. The inaccuracies are small compared with differences of the dynamic properties between the fast (red) and slow (blue) components. Furthermore, the deviation of free-energy difference does not lead to sign reversal, showing no contribution to the bias direction of the dynamics. Therefore, we can conclude that our analytical method is precise enough for assignment of the dynamic components and discussion of the NPQ molecular mechanism in LHCs.

9. Stepwise photobleaching regulated by carotenoids at discrete sites

The correlation analysis allowed us to identify the number of dynamic components and their behaviors in LHCs. However, the correlation curve estimated from the entire photon data taken from each sample is inevitably averaged over time, hence the time variations of dynamic properties can be obscured. Thus, we analyzed the photon data at a discrete time T after illumination with laser pulses.

9-1. Photobleaching progresses in steps

The fluorescence intensity distribution estimated from binned photon data at discrete T regions indicates significant changes with time, in particular in LHCSR1-V-7.5 and LHCB1-7.5 (Fig. S14), suggesting that photobleaching progresses in steps. Fig. S15 shows the time variation of the relative populations of the dynamic components. It is common across most LHCs that the population of the dominant emitter is initially reduced, suggesting that the largest energy sink undergoes photobleaching with the highest probability. Conversely, the photobleaching process is significantly different between LHCs. In LHCSR1-V-7.5 (Fig. S15*A*), firstly at $T < 50$ s, the population of the

dominant active-biased component (red) decreased, synchronized with a rise in the population of the quenched-biased component (blue). Then at $T > 300$ s, the population of the quenched component was reduced as well, and instead the unquenched contribution (orange) became dominant. The population turnover, caused by unequal photobleaching probabilities among the components, indicates multistep photobleaching processes in the order of active-biased, quenched-biased, and unquenched dynamic components. The carotenoid substitution of Zea for Vio suppressed the initial bleaching step triggering the sequential photodamage, and as a consequence made the system more robust (Fig. S15*B*). The stepwise photobleaching also occurred in LHCB1-7.5 but exhibited a different behavior, showing little population change at $T < 300$ s and then a turnover of the main emitter from the unquenched component (orange) to the quenched-biased one (red) as in Fig. S15*C*.

The correlation curves calculated by using fixed dynamic parameters somewhat deviate from the experimental profiles (Fig. S16), implying that the dynamic behavior can be perturbed by partial photobleaching. To understand the photobleaching effect, we performed the 2D-FLC analysis at different T regions with free fitting parameters. While the lifetime distribution was almost identical across all T intervals (Fig. S17), the correlation profiles changed with time (Fig. S18*A* and *C*, circles). As shown in Fig. S15*A*, LHCSR1-V-7.5 can be assumed to photobleach preferentially from the active-biased component. If the partial photobleaching induces conformational deformations in the system, the dynamic behavior of other component should be perturbed. Therefore, we carried out the correlation fitting analysis with fixed parameters of the initially-bleached component except for its relative population, and revealed that the photobleaching reverses the bias direction of the other dynamic component from active to quenched state (Fig. S18*B*, left to right).

Likewise, in LHCB1 where the unquenched component is the most fragile (Fig. S15*C*), the partial photobleaching stabilized the quenched state of the two remaining dynamic components (Fig. S18*D*). At $T = 0$ - 300 s, i.e. before photobleaching occurs (Fig. S18*D*, left), the same dynamic properties of the two components (red and blue) as those in Fig. 3*E* are enough to reproduce the correlation profiles (Fig. S18*C*, light blue). On the other hand, photobleaching of the unquenched component increased the bias toward the quenched state (Fig. S18*D*, right). Thus, in LHCs, it can be concluded that the photobleaching in a local site enhances the quenching capacity of other sites. This mechanism can prevent photodamage from rapidly spreading and therefore enable the survival of the photosynthetic system.

9-2. Stepwise photobleaching mechanism

Carotenoids at different sites are each associated with the energy sink as illustrated in Fig. S11 (7) and responsible for NPQ (see Fig. 3 and discussion in the main text). If light energy is excessively accumulated beyond the NPQ capacity, the sink is subjected to photobleaching. In LHCSR1-V-7.5 (Fig. S15*A*), the Chl *a* connecting with Vio in the Lut2 site that radiates most excitation energy underwent photodamage first (red), followed by the degradation of the Chl *a* connecting with Lut in the Lut1 site (blue), and finally the unquenched emitter became dominant (orange). Meanwhile, despite the photobleaching, the fluorescence intensity level increased (Fig. S14*A*, top), suggesting that the absorbed energy was concentrated at the unquenched site (Fig. S19*A*). In other words, the partial photobleaching changed the terminal of the energy transfer network. The continuous excitations, causing the damage to one of Chl *a*s forming an exciton cluster, would interrupt the exciton coupling. In this case, another Chl *a* cluster would serve as a substitute energy sink to compensate the photodegraded one, but would bear a double burden to deal with the excess light energy (Fig. S19*A*, center). As a result, the risk of sequential photodamages heightens (Fig. S19*A*, right).

The risk is mitigated by photobleach-induced changes in dynamic properties. The dynamics at Lut in the Lut1 site (Fig. S18*B*, blue) are initially active-biased, but after photobleaching of Chl *a* connecting with Vio in the Lut2 site the bias direction changes towards the quenched side as illustrated in Fig. S19*A*, blue circle. The local photodamage, thus, has an impact on the dynamic properties of the other surviving component, probably through a small conformational change. The photobleach-induced NPQ would impede the cascade of photodamage. However, once photobleaching occurs at the Chl *a* connecting Vio in the Lut2 site, it is only a matter of time before the system loses the NPQ function because eventually only the unquenched component is left. The poor quenching by Vio, leading to the sequential photodamages, can be reinforced by Zea binding to the Lut2 site instead of Vio, and consequently the system can be made more robust (Fig. S15*B*, red).

In contrast to LHCSR1, the unquenched site serves as the main energy sink in LHCB1-7.5 (Fig. S18*D*, orange). Therefore, photodamage preferentially takes place in the unquenched site (Fig. S15*C*, orange). This situation leads to the reduction of the risk of sequential photodamage. Additionally, as in LHCSR1, the photodegradation enhances the quenching efficiency of other sites (Fig. S18*D*, red and blue). Thus, the photobleach-induced NPQ can lower the probability of successive photodamage (Fig. S19*B*).

LHCs form a supercomplex containing the RC in photosynthetic organisms (8–10). The present study suggests that the multiple NPQ regulators in LHCs are each independently controlled by the dynamics associated with carotenoids through the lumenal ΔpH and carotenoid conversion (Fig. 3). The quenching mechanisms enable responses to both step and ramp changes in solar intensity, evening out the photoelectric conversion efficiency in the RC under any sunlight conditions (11). On the other hand, in the situation that LHCs are detached from the RC core complex, e.g.

state transitions (12), photosystem II repair cycle (13, 14), assembly of LHCs in the thylakoid membrane (15), etc., the excitation energy is accumulated within the LHCs because of the lack of usage for the photochemical reaction in the RC. If the isolated LHCs are illuminated by excess sunlight, reactive oxygen species would be generated (16, 17). In this case, the photobleach-induced NPQ mechanism can serve as a safety valve, i.e. the preferential photodamage of less quenched sites results in disconnection from dangerous energy sink as well as deformation enhancing the quenching efficiency of other surviving sites, leading to the rearrangement to a more secure energy flow network (Fig. S19). However, in LHCSR1, the unquenched site is exclusively left (Fig. S19*A*), causing a complete loss of NPQ function. Therefore, it would be difficult for LHCSR1 to participate in NPQ under extremely-high light conditions. This may explain why the LHCSR system is utilized only in algae and moss (18, 19) and offers a clue to understanding the diversity of photoprotection mechanisms across photosynthetic organisms (17, 20).

10. Supplementary Materials and Methods

Sample preparation. As previously reported (21), the LHCSR complexes were isolated from transgenic tobacco plants that express a 6His tagged ppLHCSR1 sequence. The Vio-binding form was obtained from dark-adapted plants, whereas the Zea-binding form was isolated from thylakoids incubated at pH 5 in the presence of 30 mM ascorbate for 2 hrs. The LHCB1 complexes were obtained by *in vitro* refolding of 6His-tagged LHCB1 as previously reported (22).

Single-molecule fluorescence spectroscopy. Single-molecule spectroscopy was performed as previously reported (11). Briefly, the LHCSR1 and LHCB1 complexes were diluted into a concentration of ∼pM with buffer containing 20 mM HEPES-KOH (pH 7.5) and 0.05 wt % *n*-dodecyl-α-D-maltoside and *n*-dodecyl-β-D-maltoside, respectively, for the high pH measurements, while 40 mM MES-NaOH (pH 5) and the same detergent for the low pH measurements. The sample solution also includes the enzymatic oxygen-scavenging systems; 25 nM protocatechuate-3,4-dioxygenase and 2.5 mM protocatechuic acid for the high pH measurements, and 50 nM pyranose oxidase, 100 nM catalase, and 5 mM glucose for the low pH measurements (23, 24). The LHC complexes were immobilized by the molecular interaction between a His-tag of the protein and a Ni-NTA coated on a coverslip (MicroSurfaces Inc.).

In the single-molecule fluorescence measurement, the LHCs were excited at ∼640 nm with a spatially-averaged power of ∼450 nJ/cm^2, i.e. ∼900 nJ/cm^2 at the center of the focal spot, per pulse on the sample plane. The excitation pulse was produced by filtering (ET645/30x; Chroma) a supercontinuum light, which was generated by focusing Ti:sapphire lasers (Vitara-S; Coherent; $\lambda_c = 800\,nm$, $\Delta\lambda = 70\,nm$, 20 fs pulse duration, 80 MHz repetition rate) into a nonlinear photonic crystal fiber (FemtoWhite 800; NKT Photonics). An oil-immersion objective (UPLSAPO100XO; Olympus; N.A. 1.4) was used for focusing the excitation light as well as collecting the fluorescence. The fluorescence emission was filtered (FF02-685/40-25 and FF02-675/67-25; Semrock and ET700/75m; Chroma), and then detected by an avalanche photodiode (SPCM-AQRH-15; Excelitas). The fluorescence image was constructed by scanning the sample position using a piezo-stage (Nano-LP100; Mad City Labs). The photon stream was recorded by a time-correlated single-photon counting module (PicoHarp 300; PicoQuant). The instrument response function of our setup is shown in Fig. S1*A*.

Contribution from triplet states to analysis. Singlet-triplet annihilation is the quenching of a singlet excitation upon collision with a triplet state. In LHCs, Chl triplets transfer with high efficiency to the carotenoids, where they decay on a timescale of microseconds (25–27). This timescale is longer than the duration between laser pulses for our high repetition rate (80 MHz) excitation laser, and, as a result, triplets can last for several excitation cycles. If a subsequent pulse re-excites the LHC, the new singlet state transfers among the Chls in an LHC on a femto- to picosecond time scale (28, 29), reaching the triplet and undergoing singlet-triplet annihilation. This effect has been extensively characterized LHCs, and is known to decrease the brightness of the emissive states (27, 30). In particular, in LHCII, singlet-triplet annihilation occurs on a 35 ps timescale, appearing as a component in the fluorescence decay profile (27). However, this feature appears at excitation powers exceeding 50 W/cm^2, corresponding to 658 nJ/cm^2 (27). Here, 450 nJ/cm^2 was used. As a result, the fluorescence lifetime data examined in this work does not contain effects from singlet-triplet annihilation and so the lifetime states identified from the fluorescence lifetime distribution (Fig. 2, top panels) are not influenced by triplet states, although their corresponding intensities likely decrease somewhat due to singlet-triplet annihilation.

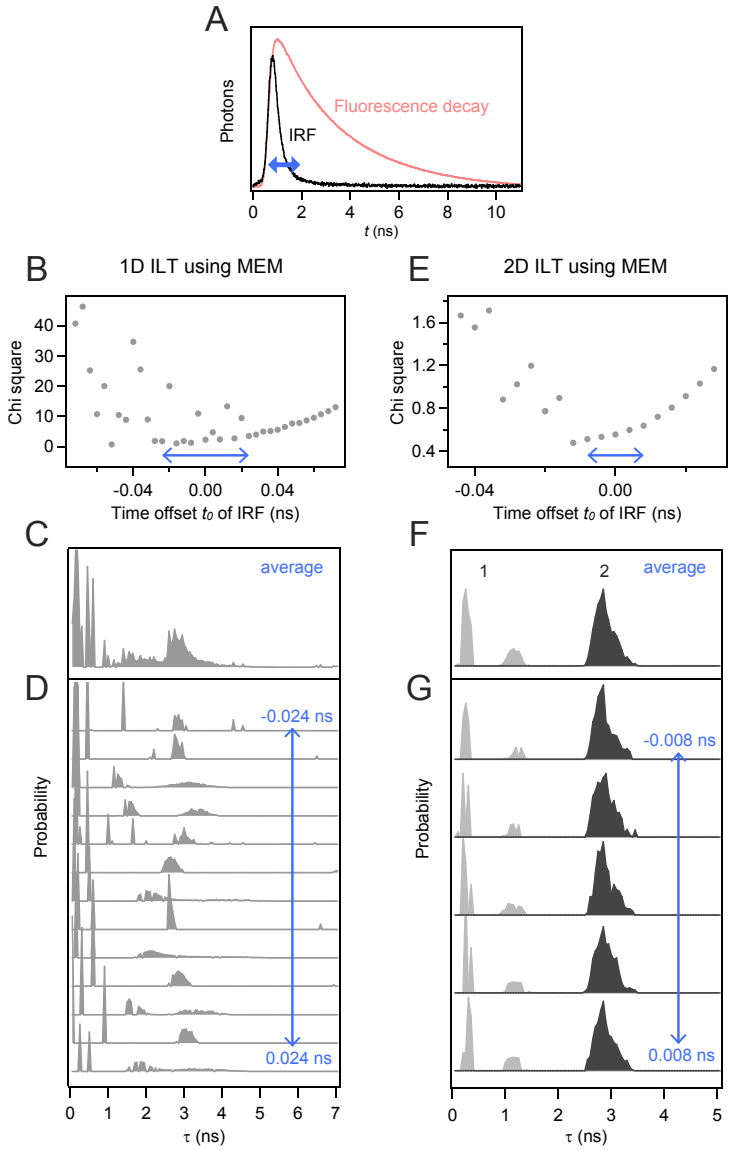

Figure S1: Sensitivity of 1D/2D-ILT to IRF time offset. **(*A*)** Fluorescence decay profile of LHCSR1 with Vio at pH 7.5 (red) and experimentally-measured instrument response function, IRF (black). The relative position of IRF is adjusted by changing the time offset t_0, defined in Eq. [2], as indicated by the blue arrow. **(*B*)** Fitting error in the lifetime distribution analysis, estimated by the 1D-ILT of the fluorescence decay. The chi-square defined by Eq. [4] was calculated at various time offsets t_0 of the IRF. **(*C, D*)** Averaged lifetime distribution **(*C*)** and thirteen lifetime distributions used for the averaging **(*D*)**, corresponding to the results with low chi-squares in the range of $t_0 = -0.024 \sim 0.024$ ns as indicated by an blue arrow in ***B***. **(*E*)** Fitting error in the 2D-FLC analysis performed with various values of t_0 for the IRF. **(*F, G*)** Averaged lifetime distribution **(*F*)** and five lifetime distributions used for the averaging **(*G*)**, corresponding to the results with low chi-squares in the range of $t_0 = -0.008 \sim 0.008$ ns as indicated by the blue arrow in ***E***. The gray and black distributions are ascribed to discrete states 1 and 2, respectively.

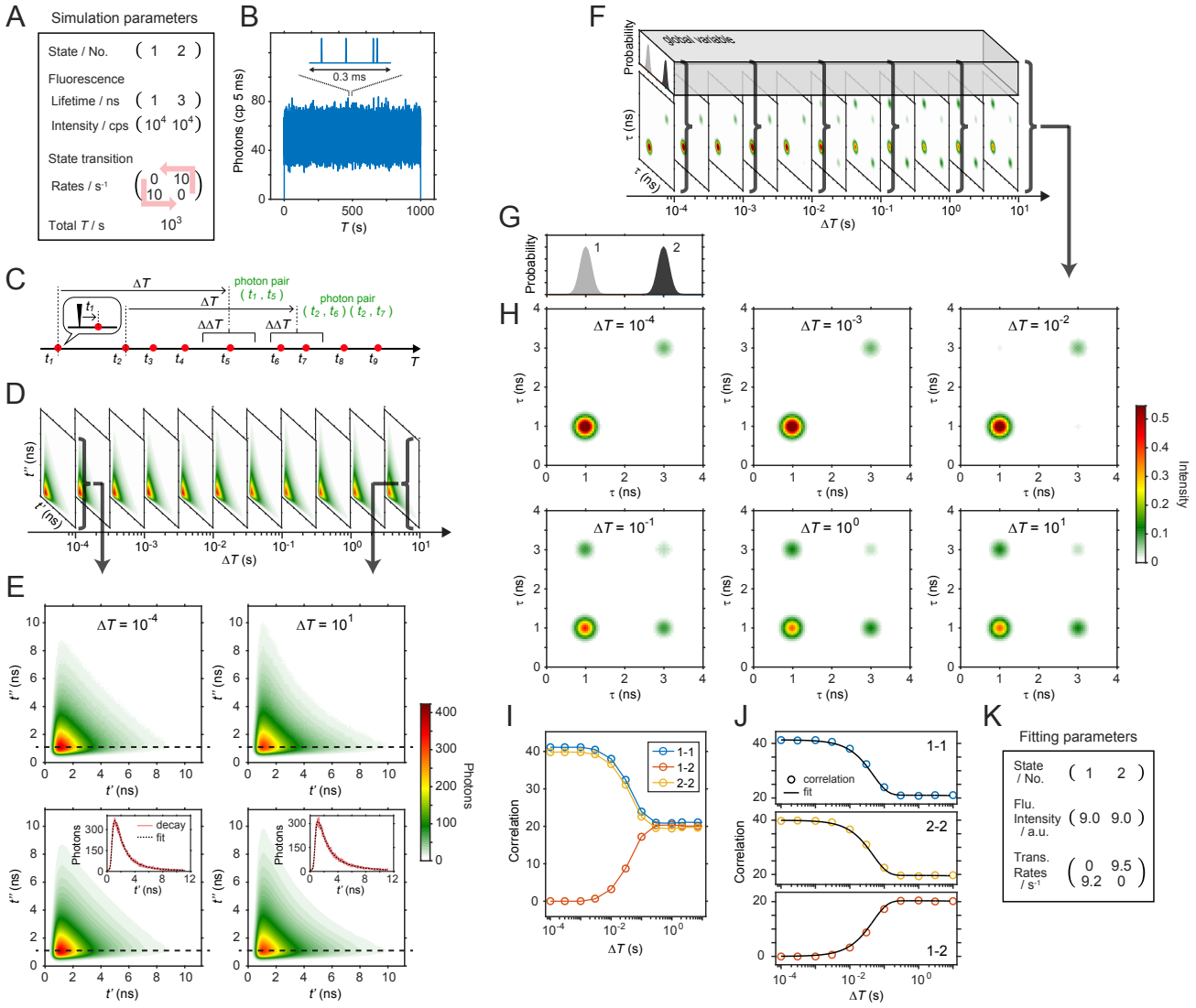

Figure S2: Procedure for 2D-FLC analysis. **(*A*)** Monte Carlo simulation parameters used to generate an artificial photon stream, where a simple two-state system exhibiting different fluorescence lifetimes and the same intensities was assumed. The dynamics rates were input as a rate matrix, of which the element K_{ji} indicates the rate of the transition from state i to j at $i \neq j$ and of the molecule being lost at $i = j$. **(*B*)** Time trace of photon counts estimated by binning the photon stream in intervals of 5 ms. In reality, photons are discrete as shown in the time axis in the inset. **(*C*)** Schematic of data collection to construct the 2D-FD map from the photon stream, where the red circles indicate detected photons and the black triangle in inset represents a time point of the excitation pulse. Each photon is characterized by two time parameters; macro time T and micro time t, corresponding to the photon detection time with respect to the measurement start and excitation pulse, respectively. Photon pairs separated by the time interval ΔT, in which all photons within the time window $\Delta\Delta T$ were picked up as second photons, are characterized by a time data set (t_n, t_m). **(*D*)** The 2D-FD maps at ΔTs from 10^{-4} to 10^{1} s, constructed by calculating a histogram of (t_n, t_m) given from all photon pairs at each ΔT. **(*E*)** Examples of the 2D-FD maps at $\Delta T = 10^{-4}$ (left) and 10^{1} s (right), compared with fitting results estimated using 2D-MEM in the 2D-FLC analysis (lowers). The inset indicates the fluorescence decay profile sliced along the dotted line in the upper (red line) and lower 2D-FD maps (black dotted line). **(*F*)** Fluorescence lifetime distributions of two lifetime states and 2D-FLC between them estimated by ILT of 2D-FD at various ΔTs from 10^{-4} to 10^{1} s. The lifetime distribution, set as a global variable, is independent on ΔT, whereas the 2D-FLC, set as a local variable, is given at each ΔT. **(*G-I*)** Fluorescence lifetime distribution **(*G*)**, examples of the 2D-FLC map at each ΔT **(*H*)**, and correlation function **(*I*)**, corresponding to the matrix A, $\tilde{M}(\Delta T)$, and $G^n(\Delta T)$, respectively, estimated by fitting using 2D-MEM in the 2D-FLC analysis. The gray and black distributions in **g** are ascribed to distinct states 1 and 2, respectively. The correlation function in ***I*** was given by the normalization of $G(\Delta T)$ as described in Eq. [13], and is composed of auto-correlations of each state (labeled 1-1 and 2-2) and cross-correlation between the different states (labeled 1-2). **(*J*)** Fitting correlation curves, indicated by black lines, calculated using Eq. [19]. **(*K*)** Fitting parameters including the relative fluorescence intensity of each state and rate matrix of transition between the states.

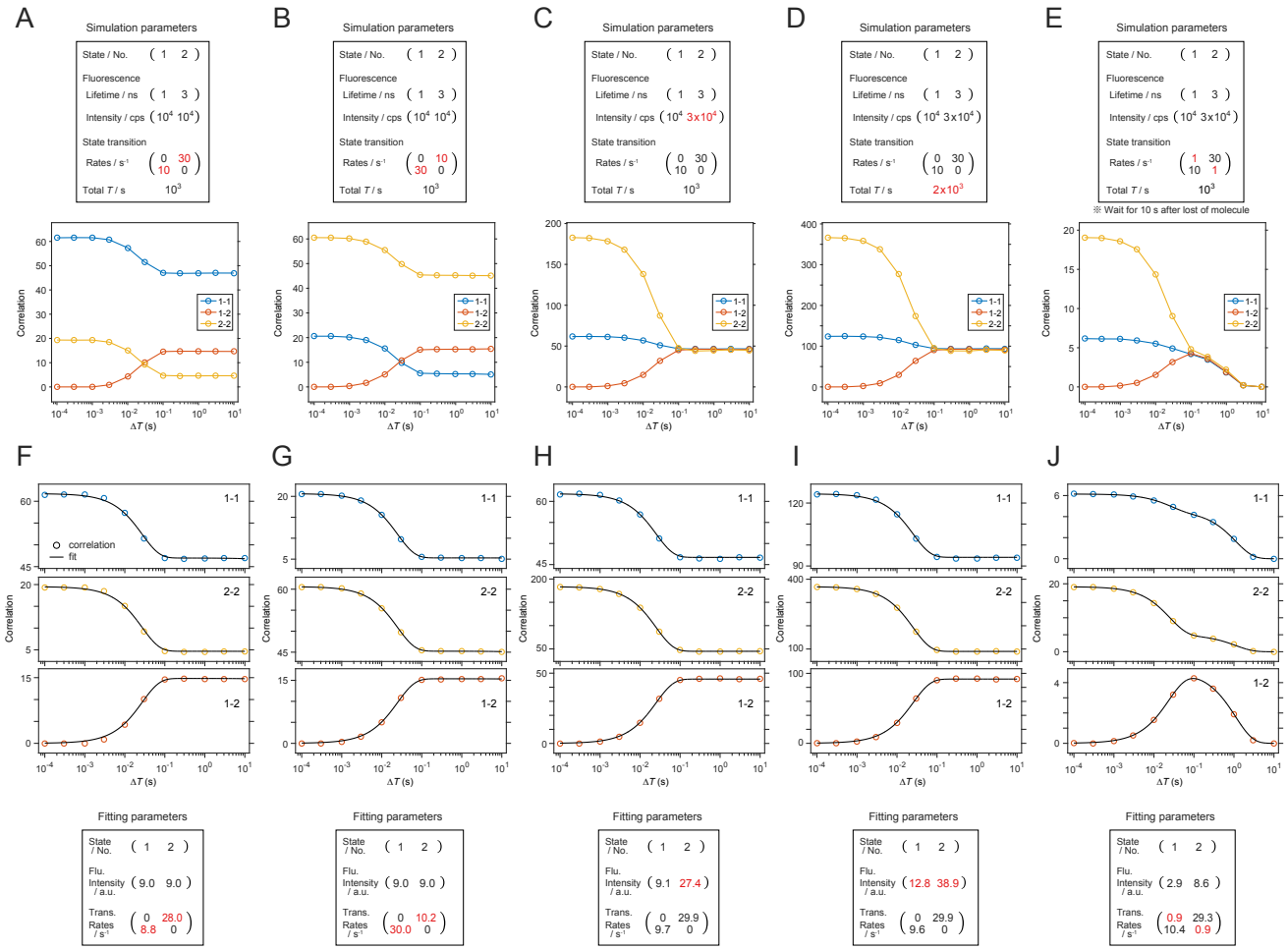

Figure S3: Demonstration of 2D-FLC analysis using artificial photon streams, which were generated with simple two-state models under various conditions. (***A-E***) Biased dynamics to state 1 (***A***), inversely-biased dynamics to state 2 (***B***), different fluorescence intensities between state 1 and 2 (***C***), twice longer measurement time (***D***), and molecular loss that corresponds to photobleaching or molecular diffusion (***E***). These specific conditions were characterized by the parameter in red in the upper panel. The correlation function in the lower panel was estimated by the 2D-FLC analysis of each photon stream. (***F-J***) Fitting correlation curves indicated by black lines in the upper panel, which were given by the global fitting of each correlation function in ***A-E***, respectively, using Eq. [19]. The parameters in the lower panel, given by the correlation fitting, indicate the relative fluorescence intensity of each state and the rate matrix of transition between the states.

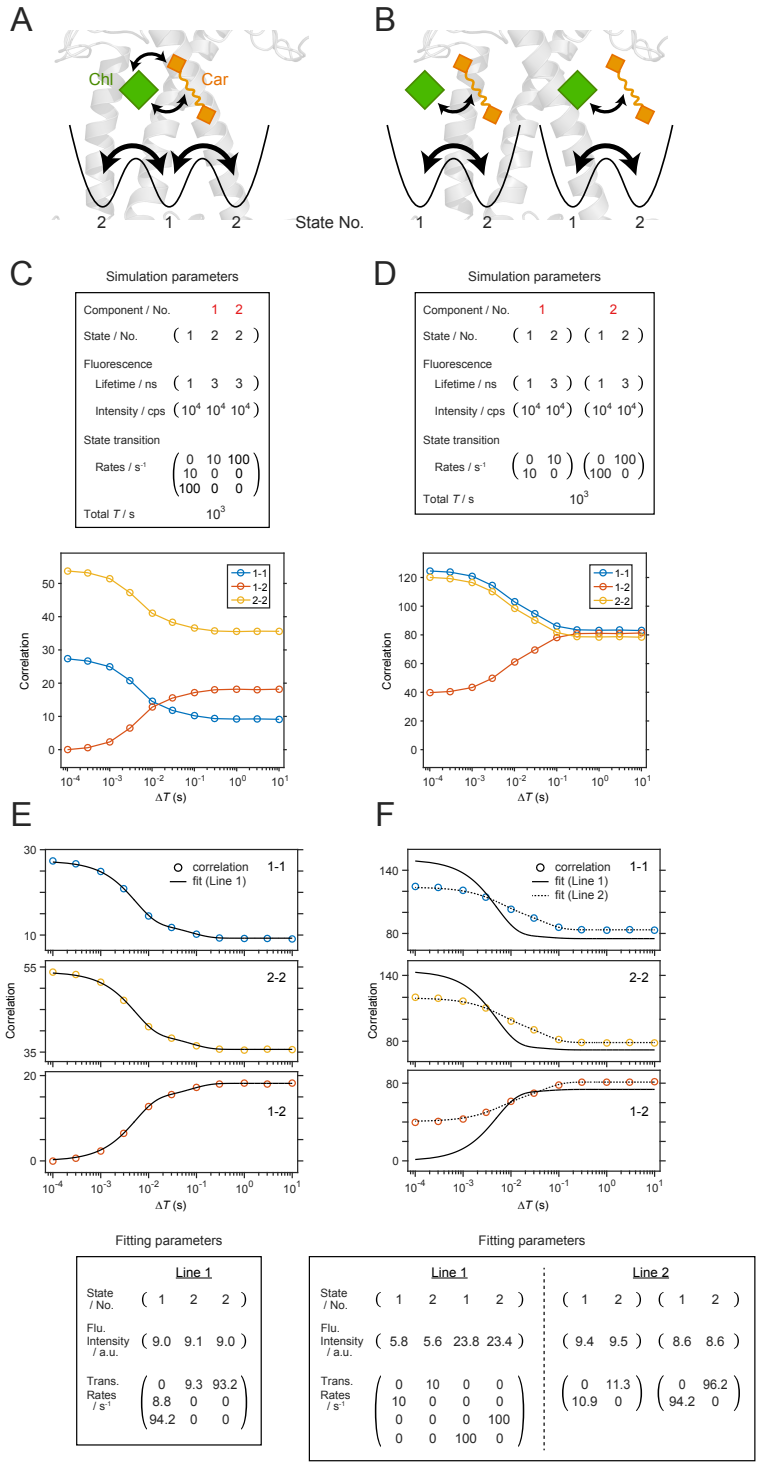

Figure S4: Identification of multiple independent dynamics based on 2D-FLC analysis. (*A*, *B*) Schematic of a protein system comprised of two components exhibiting sequential **(*A*)** and independent dynamics **(*B*)**. **(*C*)** Parameters used in the Monte Carlo simulation of the photon stream for the sequential dynamic system, reproduced by transitions between three states, one short and two long lifetime states (upper), and the correlation function estimated by the 2D-FLC analysis (lower). **(*D*)** Simulation parameters for the multiple independent processes given by the combination of two dynamics between short and long lifetime states (upper), and the estimated correlation function (lower). **(*E*, *F*)** Fitting correlation curves in the upper panel, which were calculated for the systems as illustrated in ***A*** and ***B***, respectively, using Eq. [19] (solid lines) and Eq. [20] (dotted lines). These fitting curves were calculated from the parameters listed as Line1 and Line2, respectively, in the lower panels.

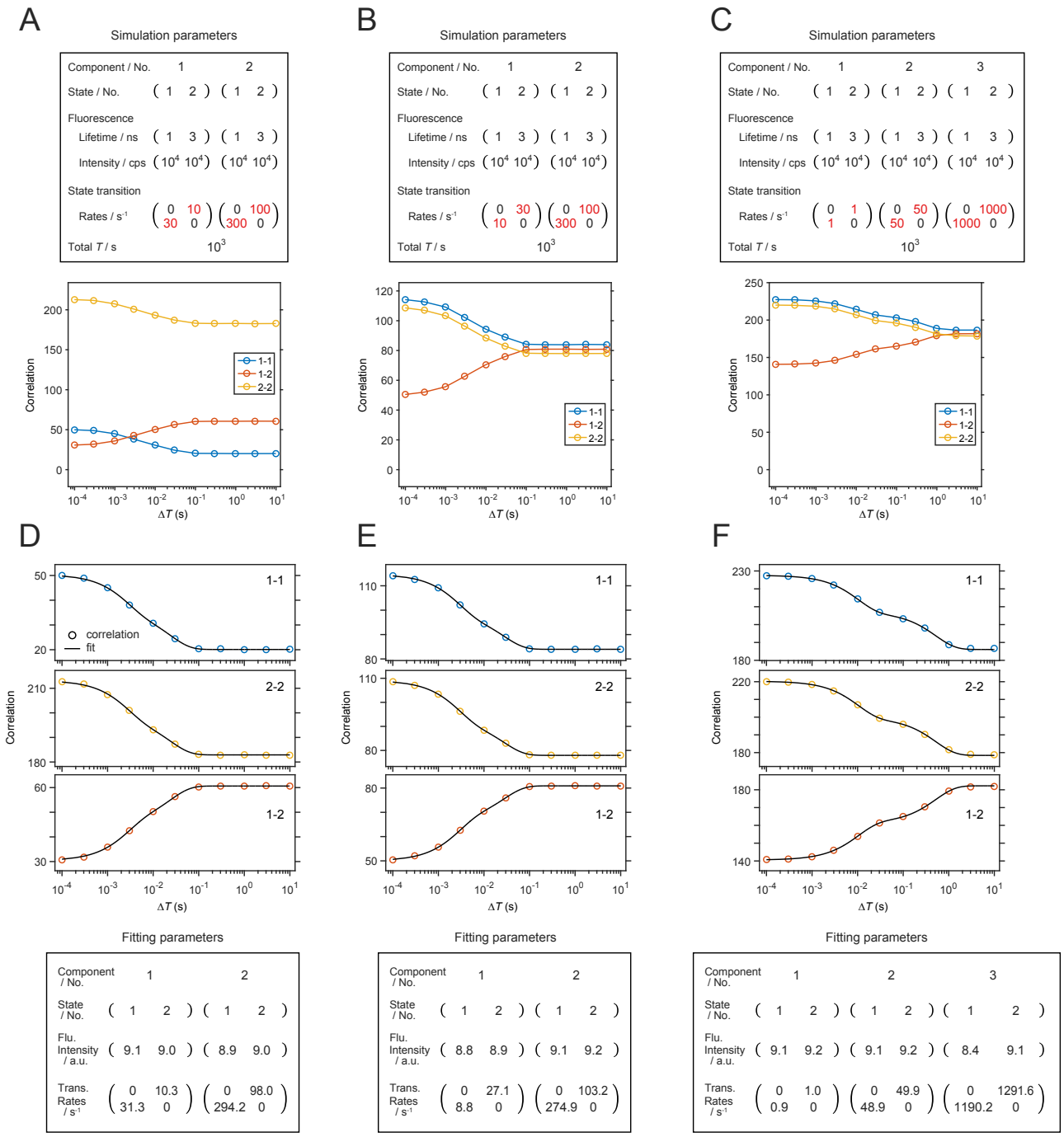

Figure S5: Demonstration of correlation analysis of multiple dynamics comprised of independent components, each of which was represented by a two-state system. (*A-C*) Monte Carlo simulation of photon streams to reproduce various dynamics of multiple independent components; two components with dynamics in parallel **(*A*)** and antiparallel **(*B*)**, and three dynamics components **(*C*)**. The photon stream calculated based on the parameters (upper) was analyzed by the 2D-FLC algorithm to estimate the correlation function (lower). **(*D-F*)** Fitting correlation curves indicated by black lines in upper panel, which were given by the global fit of each correlation function in ***A-C***, respectively, using Eq. [20]. The parameters in the lower panel indicate the relative fluorescence intensity of each state and the rate matrix of transition between the states.

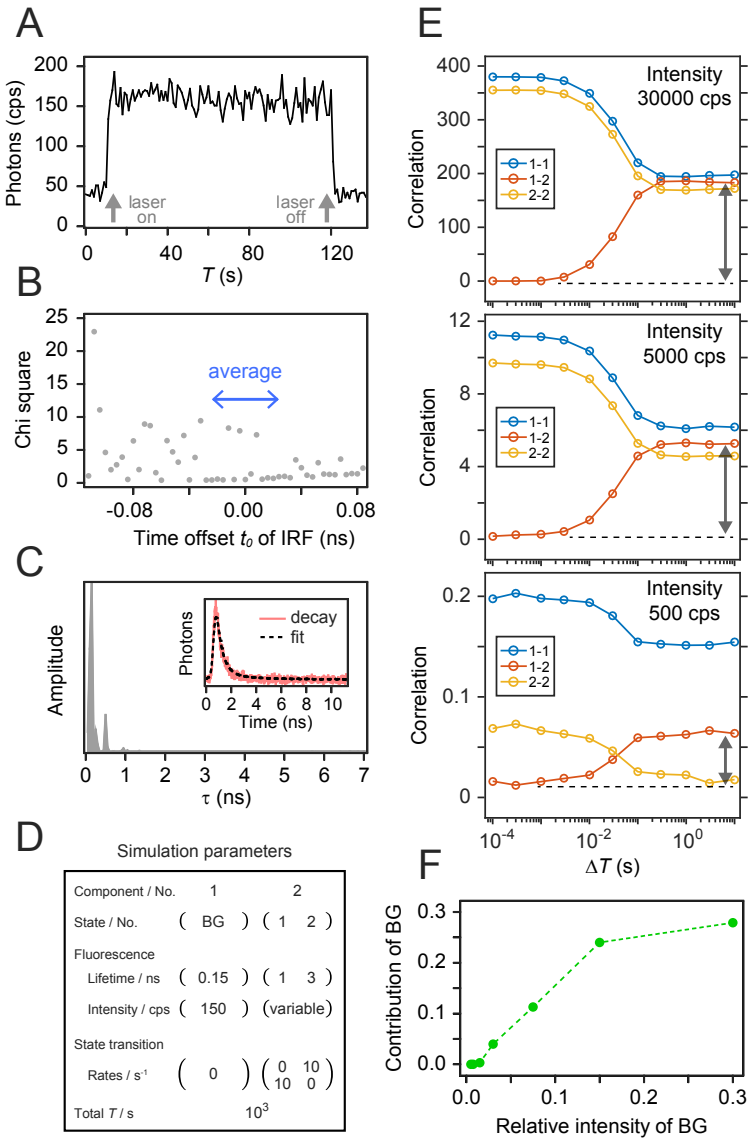

Figure S6: Contribution of background to the base correlation in cross-correlation. (***A***) Time trace of the signal intensity measured on the dark (background) area in a fluorescence image. (***B***) Fitting error of the lifetime distribution analysis with 1D-ILT, estimated at various IRF time offsets. (***C***) Lifetime distribution of the background signal, which is an average of thirteen fitting results with low chi-square as indicated by the blue arrow in ***B***. The inset shows the experimental decay profile (red line) and averaged fitting curve (black dotted line). (***D***) Parameters used for the Monte Carlo simulation of a photon stream based on the two-states model with background (BG) contribution. The intensity and lifetime of the BG were given experimentally from ***A*** and ***C***, respectively. The intensity of a dynamic component other than the BG varied from 30000 to 500 cps, i.e. changing the ratio of the intensity of the BG to the dynamic component from 0.005 to 0.3. (***E***) Correlation function estimated by 2D-FLC analysis of each photon stream. (***F***) Relationship between the intensity ratio and contribution of BG to cross-correlation, which was estimated as a ratio of the base correlation at $\Delta T = 10^{-4}$ s to the correlation change between $\Delta T = 10^{-4}$ and 10^{1} s in the cross-correlation curve as indicated by the black arrows in ***E***.

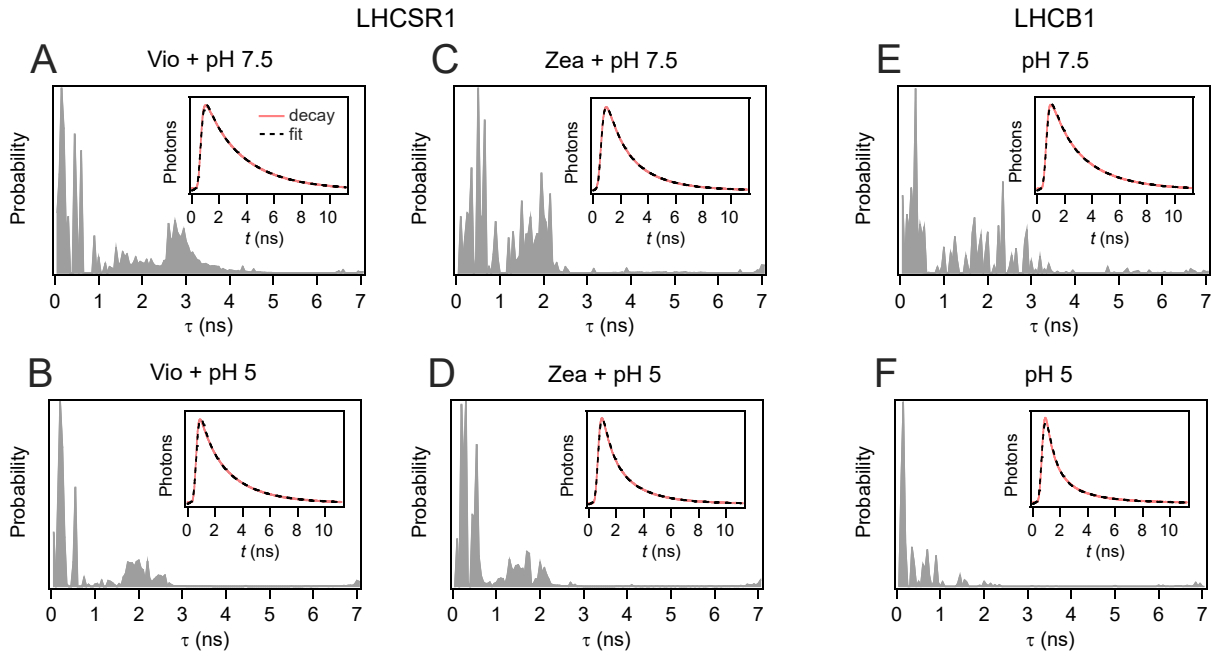

Figure S7: Fluorescence lifetime distribution in LHCSR1 and LHCB1. (***A-F***) Fluorescence lifetime distributions estimated by 1D-ILT in LHCSR1 with Vio at pH 7.5 (***A***) and pH 5 (***B***), Zea-enriched LHCSR1 at pH 7.5 (***C***) and pH 5 (***D***), and LHCB1 at pH 7.5 (***E***) and pH 5 (***F***). The inset indicates an experimental decay profile (red line) and fitting curve estimated by 1D-ILT with MEM (black dotted line). As shown in Fig. S1*B-D*, thirteen distributions calculated with different time offsets for the IRF were averaged.

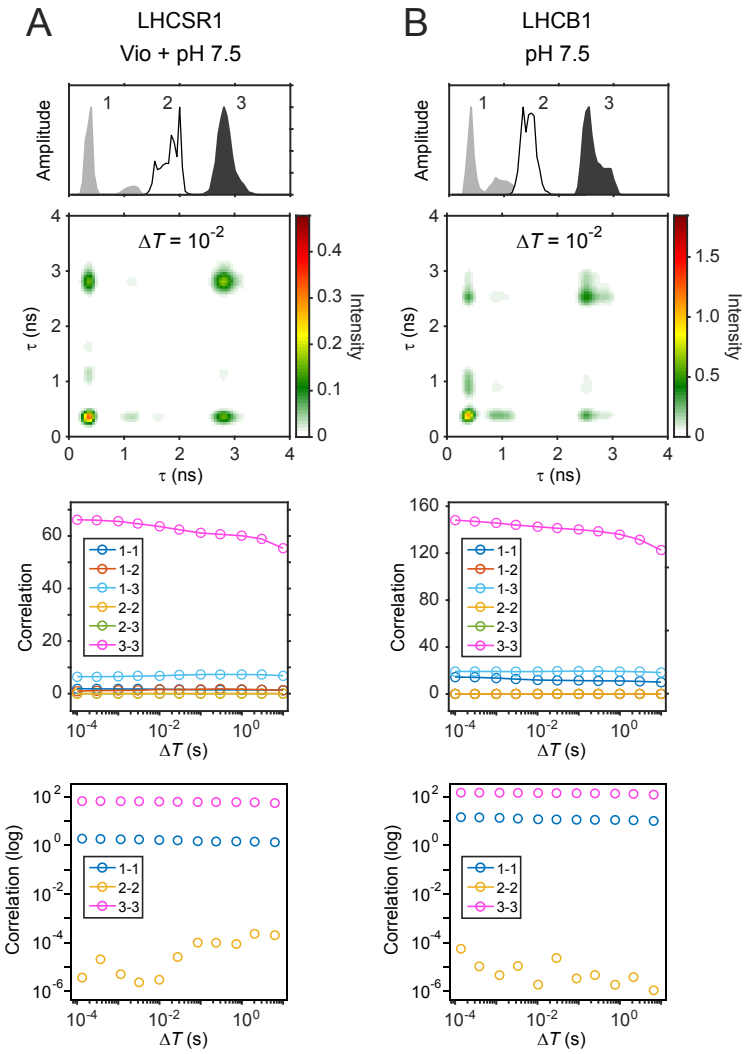

Figure S8: 2D-FLC analysis with three lifetime states. (*A*, *B*) Lifetime distribution (top), 2D-FLC map at $\Delta T = 10^{-2}$ s (upper middle), correlation function (lower middle), and auto-correlation of each state in log scale (bottom) were calculated by the 2D-FLC analysis with three lifetime states in LHCSR1-V-7.5 **(*A*)** and LHCB1-7.5 **(*B*)**. The lifetime distributions estimated by 1D-ILT in LHCSR1-V-7.5 and LHCB1-7.5 are somewhat broad, compared with those in other samples (Fig. S7). Thus, we checked if the two lifetime states at around 3 and < 1 ns, illustrated in Fig. 2*A* and *E*, are enough to analyze these samples. As shown in the lifetime distribution (top), a third lifetime state at around 1.8 ns, i.e. state 2, was added to cover the whole region of the lifetime distribution in Fig. S7*A* and *E*. The 2D-FLC map (upper middle) shows no correlation for the state 2, and also the auto-correlation of the state 2 (bottom, orange) indicates no contribution from the state 2 at all ΔTs. Therefore, we concluded that two lifetime states other than the state 2 are dominant.

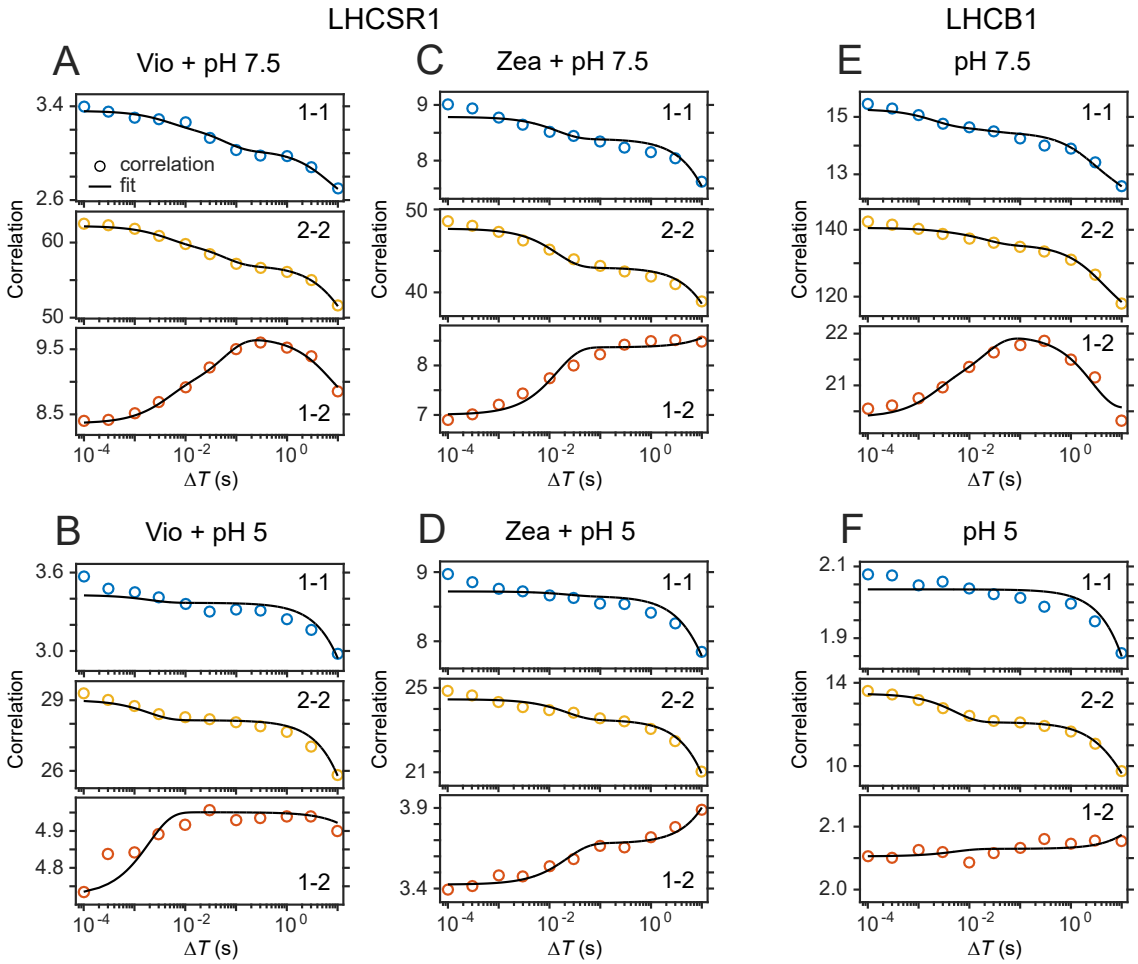

Figure S9: Correlation analysis of single LHCSR1 and LHCB1 under different conditions. (*A*-*F*) Correlation function $G^n(\Delta T)$ estimated from the 2D-FLC analysis of single LHCSR1s with Vio at pH 7.5 **(*A*)** and pH 5 **(*B*)**, Zea-enriched LHCSR1 at pH 7.5 **(*C*)** and pH 5 **(*D*)**, and LHCB1 at pH 7.5 **(*E*)** and pH 5 **(*F*)**. The correlation curves for auto- (1-1 and 2-2) and cross-correlations (1-2) correspond to diagonal and off-diagonal elements of $G^n(\Delta T)$, respectively. The black line indicates a fitting curve calculated using the model function $G^s(\Delta T)$ given by Eq. [20].

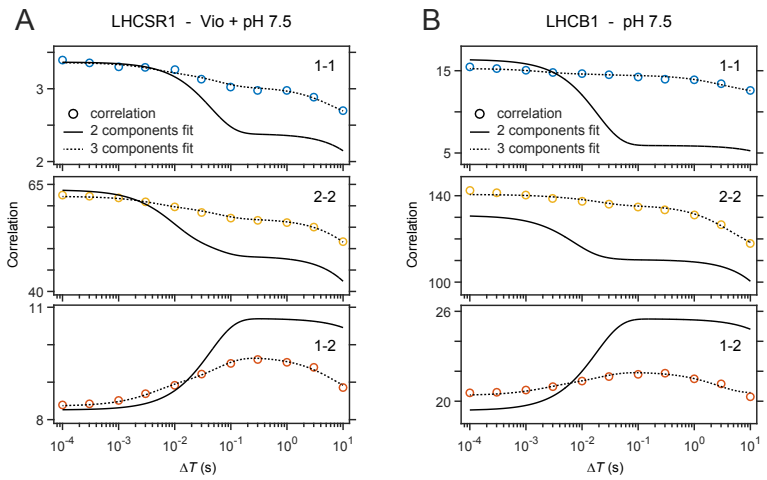

Figure S10: Correlation fitting analysis with multiple dynamic components. (*A*, *B*) Comparison between fitting curves calculated from two (solid line) and three (dotted line) dynamic components in LHCSR1-V-7.5 **(*A*)** and LHCB1-7.5 **(*B*)**. The auto- (1-1 and 2-2) and cross-correlations (1-2) were globally fitted.

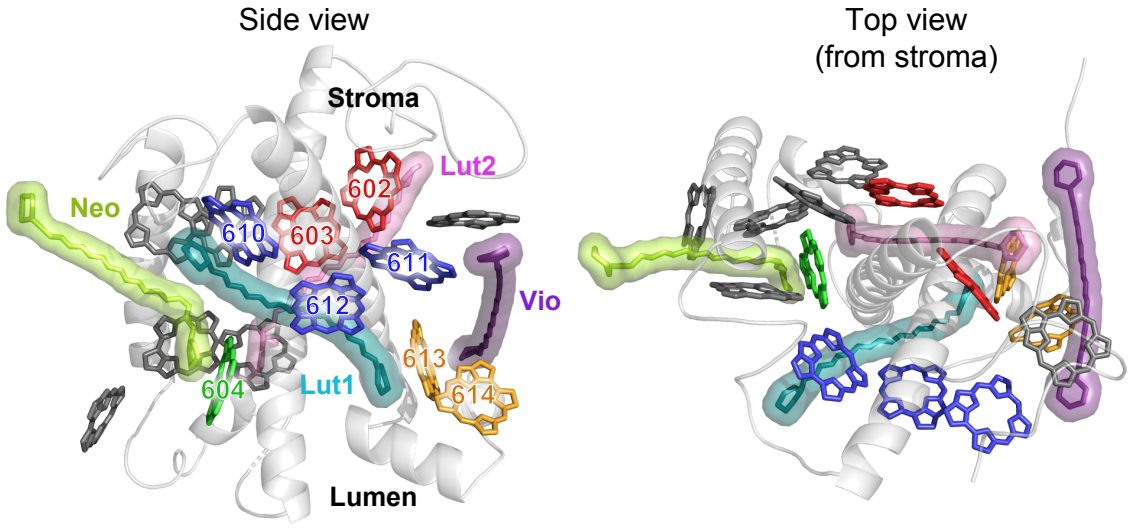

Figure S11: Crystal structure of LHCII monomer. Pigment arrangements of Chl and carotenoid in LHCII monomer, in which the protein scaffold and all Chl *b*s are shown in light gray and black, respectively. Chl *a*s, numbered according to the LHCII crystal structure (7), are grouped into one trimer of Chl *a*610-611-612 (blue), two dimers of Chl *a*602-603 (red) and Chl *a*613-614 (orange), and one monomer of Chl *a*604 (green). Four carotenoids are Lut1 (cyan), Lut2 (pink), Neo (light green), and Vio (violet) in each binding site. The pH-sensing residues are suggested to be on the lumenal side.

LHCSR1

Vio + pH 7.5

Component	1		2		3	
Fluorescence						
Lifetime state	1	2	1	2	1	2
Lifetime	0.52	2.89	0.52	2.89	0.52	2.89
Intensity	0.12	0.48	0.13	0.57	0.20	0.55
Transition rates						
Lifetime state Final \ Initial	1	2	1	2	1	2
1	0.16	11	0.03	30	< 0.001	0.001
2	6	0.16	219	0.03	0.001	< 0.001
Population	0.65	0.35	0.12	0.88	0.53	0.47
Free-energy difference	125		-414		25	

Zea + pH 7.5

Component	1		2	
Fluorescence				
Lifetime state	1	2	1	2
Lifetime	0.69	2.26	0.69	2.26
Intensity	0.13	0.44	0.16	0.65
Transition rates				
Lifetime state Final \ Initial	1	2	1	2
1	0.03	60	0.005	0.007
2	10	0.03	0.006	0.005
Population	0.85	0.15	0.56	0.44
Free-energy difference	365		49	

Vio + pH 5

Component	1		2	
Fluorescence				
Lifetime state	1	2	1	2
Lifetime	0.47	2.39	0.47	2.39
Intensity	< 0.01	0.83	0.15	0.55
Transition rates				
Lifetime state Final \ Initial	1	2	1	2
1	< 0.001	0.009	0.01	506
2	0.003	< 0.001	9	0.01
Population	0.76	0.24	0.98	0.02
Free-energy difference	239		840	

Zea + pH 5

Component	1		2	
Fluorescence				
Lifetime state	1	2	1	2
Lifetime	0.42	2.09	0.42	2.09
Intensity	0.11	0.98	0.14	0.54
Transition rates				
Lifetime state Final \ Initial	1	2	1	2
1	< 0.001	0.012	0.03	44
2	0.002	< 0.001	1	0.03
Population	0.84	0.16	0.98	0.02
Free-energy difference	350		787	

LHCB1

pH 7.5

Component	1		2		3	
Fluorescence						
Lifetime state	1	2	1	2	1	2
Lifetime	0.62	2.70	0.62	2.70	0.62	2.70
Intensity	0.10	0.45	0.15	0.16	0.43	0.92
Transition rates						
Lifetime state Final \ Initial	1	2	1	2	1	2
1	0.30	12	0.44	357	0.006	< 0.001
2	37	0.30	160	0.44	0.001	0.006
Population	0.24	0.76	0.69	0.31	0.36	0.64
Free-energy difference	-237		168		122	

pH 5

Component	1		2	
Fluorescence				
Lifetime state	1	2	1	2
Lifetime	0.33	2.02	0.33	2.02
Intensity	0.11	1.00	< 0.01	0.19
Transition rates				
Lifetime state Final \ Initial	1	2	1	2
1	0.010	0.004	0.11	73
2	< 0.001	0.010	117	0.11
Population	0.95	0.05	0.39	0.61
Free-energy difference	615		-97	

Lifetime, transition rates, and free-energy difference are described in ns, 1/s, and cm^{-1}, respectively. Fluorescence intensities are normalized values in arbitrary unit. Population indicates relative populations between state 1 and 2 for each dynamic component.

Table S1: Dynamic properties estimated by the correlation fitting analysis. The fluorescence intensity and transition rates from initial state (column-wise) to final state (row-wise) were estimated in LHCSR1 with Vio (top) and Zea (middle) and LHCB1 (bottom) at pH 7.5 (left) and 5 (right) by global fitting of the correlation function as shown in Fig. S9. The population and free-energy difference were given by Eqs. [18] and [23], respectively. The fluorescence intensity shows a relative intensity that was first normalized with the total measurement time T for each sample and then with a scaling factor to set the maximum intensity to be 1.

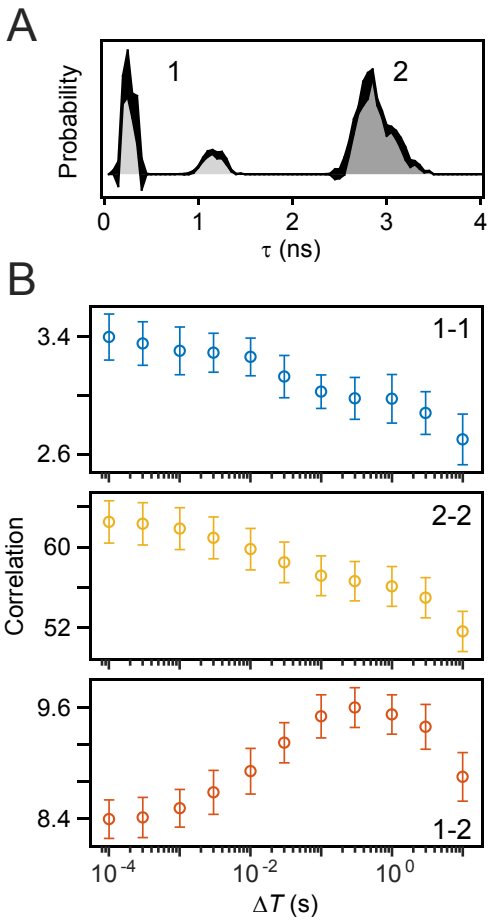

Figure S12: Standard deviations for the 2D-FLC analysis, estimated from five randomly-grouped complexes of LHCSR1-V-7.5. Standard deviations estimated from five trials of the 2D-FLC analysis are shown in the lifetime distribution (***A***, black area) and correlation curves (***B***, error bars). The peaks in light and dark gray in ***A*** correspond to lifetime distributions of state 1 and 2, respectively. The deviations of auto- and cross-correlation (1-1, 2-2, and 1-2) in ***B*** were calculated to be 4.7, 3.5, and 2.5%, respectively, on average.

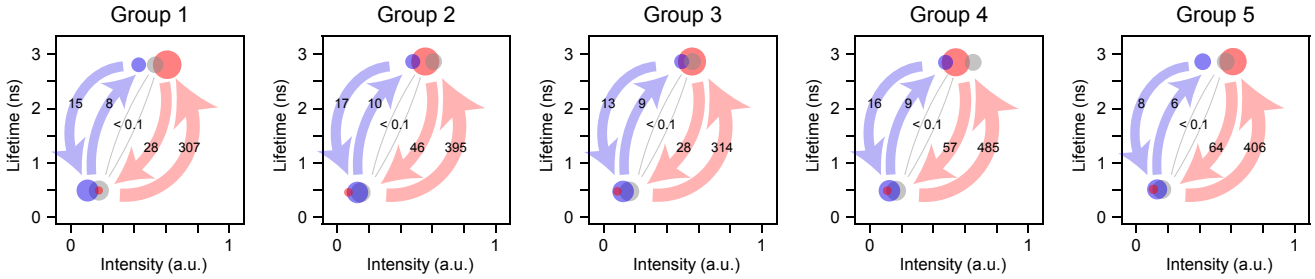

Figure S13: Variations in the dynamic properties estimated by the correlation fitting analysis for the five randomly-grouped complexes of LHCSR1-V-7.5. Five correlation functions were estimated by the 2D-FLC analysis of five different groups of LHCSR1-V-7.5 complexes. The correlation fitting analysis of each correlation function was performed with three components as in Fig. 3*A*. The dynamic properties of the components, estimated from each group, are illustrated as a diagram in panels ***1-5***. Transitions take place between short and long lifetime states, corresponding to quenched (Q) and active (A) states, respectively. The short and long lifetimes were mean values of τ estimated from the lifetime distribution of states 1 and 2, respectively. Circle size and arrow thickness exhibit the relative population and transition rate between the two states, respectively. The number on the arrow indicates the transition rate in 1/s. Standard deviations of the dynamic properties, estimated from these five fitting results, are summarized in Table S2.

LHCSR1 + violaxanthin + pH 7.5

Component	1		2		3	
			Fluorescence			
Lifetime state	1	2	1	2	1	2
Lifetime	0.52 ± 0.02	2.89 ± 0.02	0.52 ± 0.02	2.89 ± 0.02	0.52 ± 0.02	2.89 ± 0.02
Intensity	0.12 ± 0.01	0.48 ± 0.03	0.13 ± 0.04	0.57 ± 0.03	0.20 ± 0.01	0.55 ± 0.04
			Transition rates			
Lifetime state Final \ Initial	1	2	1	2	1	2
1	0.16 ± 0.02	11 ± 3	0.03 ± 0.01	30 ± 15	< 0.0010 ± 0.0001	0.0010 ± 0.0001
2	6 ± 1	0.16 ± 0.02	219 ± 60	0.03 ± 0.01	0.0010 ± 0.0001	< 0.0010 ± 0.0001
Population	0.65 ± 0.03	0.35 ± 0.03	0.12 ± 0.02	0.88 ± 0.02	0.53 ± 0.03	0.47 ± 0.03
Free-energy difference	125 ± 27		-414 ± 44		25 ± 24	

Lifetime, transition rates, and free-energy difference are described in ns, 1/s, and cm^{-1}, respectively. Fluorescence intensities are normalized values in arbitrary unit. Population indicates relative populations between state 1 and 2 for each dynamic component. Error indicates ± S.D. estimated from five randomly-grouped molecules.

Table S2: Standard deviations of the dynamic properties estimated by the correlation fitting analysis, performed for the five randomly-grouped complexes of LHCSR1-V-7.5.

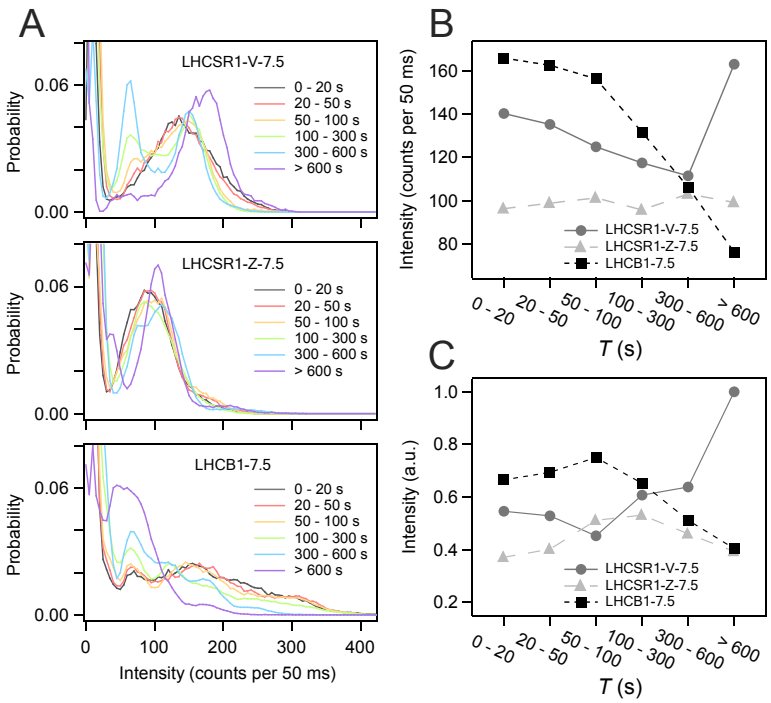

Figure S14: Time variation of the fluorescence intensity. **(*A*)** The fluorescence intensity distribution at discrete interval of T, which is an elapsed time after starting the excitation, in LHCSR1-V-7.5 (top), LHCSR1-Z-7.5 (middle) and LHCB1-7.5 (bottom). The histogram of photon counts binned at 10 ms was estimated from photon stream data separated by each T interval. The background level in our setup was ∼200 cps on average, and thus the steep peak at intensity less than 25 counts per 50 ms (= 500 cps) is ascribed to the background light. The probability was normalized so that the sum at $>$ 500 cps is equal to 1. **(*B*)** Average intensity at each T interval, estimated from the distribution at $>$ 500 cps in LHCSR1-V-7.5 (gray circle), LHCSR1-Z-7.5 (light gray triangle) and LHCB1-7.5 (black square). **(*C*)** Total intensity at each T interval, estimated by the correlation analysis shown in Figs. S15 and S16. The intensity on the vertical axis was calculated by summing the average intensities of two dynamic components in LHCSR1-Z-7.5 (light gray triangle) as well as the intensity of active state of static component in LHCSR1-V-7.5 (gray circle) and LHCB1-7.5 (black square). The time variations estimated by the binning **(*B*)** and correlation **(*C*)** analysis both show that the intensity finally increases in LHCSR1-V-7.5, exhibits little change in LHCSR1-Z-7.5, and gradually decreases in LHCB1-7.5. These behaviors support the stepwise photobleaching model suggested in Fig. S19.

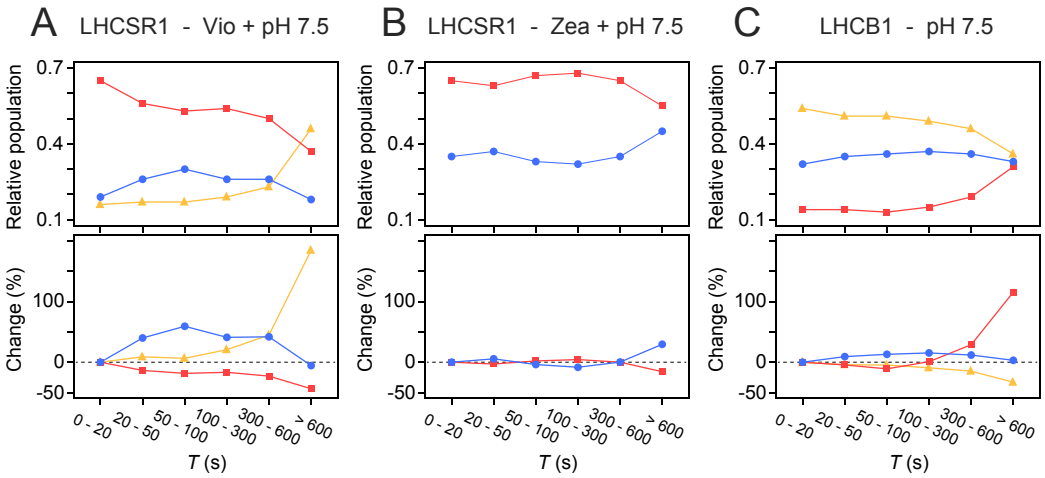

Figure S15: Time dependence of dynamic component population upon excitation. (*A*-*C*) Relative population of the dynamic component (upper) and rate of change (lower) at different intervals of T, the elapsed time after starting excitation, in LHCSR1 with Vio **(*A*)** and Zea **(*B*)** and LHCB1 **(*C*)** at pH 7.5. The red and blue curves indicate time variations in the relative population of the dynamic components illustrated in red and blue, respectively, in Fig. 3. The orange curve corresponds to the population of active state of the gray static component in Fig. 3, i.e. the relative population of unquenched emitters. The relative population was estimated as the following: First, correlation profiles were calculated using the 2D-FLC analysis at each T interval, where the lifetime distribution was fixed to be the same as that in Fig. 2. Then, the correlation function was fitted using the model function, in which fitting parameters of the fluorescence intensity and transition rate were fixed to be the same as those in Fig. 3 for the dynamic components except for the static one (All fitting results were shown in Fig. S16). From this, we obtained the abundance ratio of the components. Finally, the relative population of each component was given as the fluorescence intensity ratio estimated by multiplying the abundance ratio by the fluorescence intensity, which is an intensity of active state (orange) or an average of active and quenched states (red and blue). Accordingly, the relative population indicates a relative amount of fluorescence photons radiated from each component, reflecting a quantity of light energy that is accumulated at each emitter and not quenched by carotenoids. The fluorescence intensity distribution, estimated from binned photon data independently on the correlation analysis, is also shown in Fig. S14*A* and *B*.

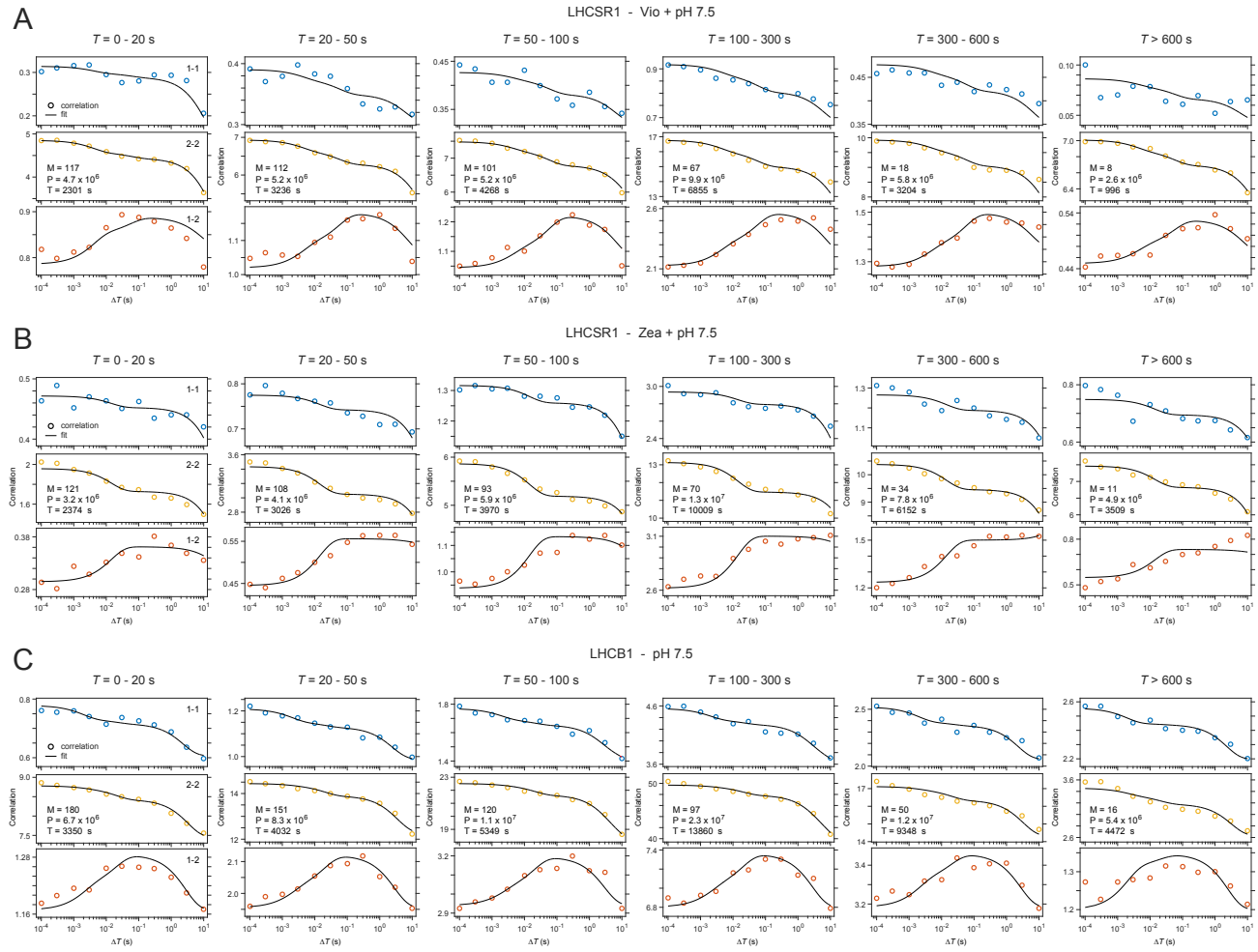

Figure S16: Correlation fitting analysis for photon data at discrete interval of T, which is an elapsed time after starting the excitation. (*A*-*C*) The correlation profiles (circles) were estimated by the 2D-FLC analysis for photon data at each time interval in LHCSR1-V-7.5 **(*A*)**, LHCSR1-Z-7.5 **(*B*)**, and LHCB1-7.5 **(*C*)**, where the lifetime distribution was fixed to be the same as that in Fig. 2*A*, *C*, and *E*, top, respectively. Then, they were fitted with a model function taking into account three dynamic components (solid lines), where the two dynamic components were treated as constants except for their abundance ratios while the other static one as a free component. The relative populations of the components are shown in Fig. S15.

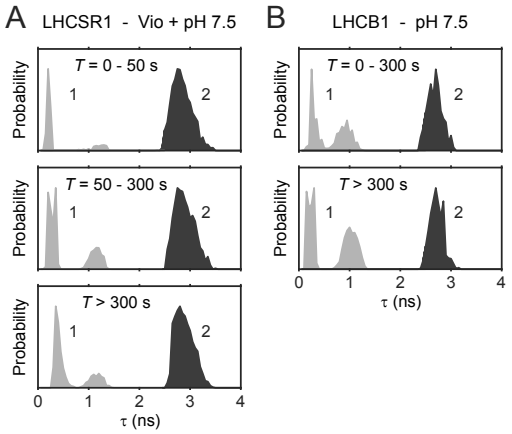

Figure S17: Time variation of the fluorescence lifetime distribution. (*A*, *B*) Fluorescence lifetime distribution estimated from the 2D-FLC analysis with two lifetime states for photon data at discrete interval of T, which is an elapsed time after starting the excitation, in LHCSR1-V-7.5 (***A***) and LHCB1-7.5 (***B***). The correlation profiles at different time regions, obtained from this analysis, were followed by the fitting analysis as discussed in Fig. S18 and Section 9 in Supplementary text.

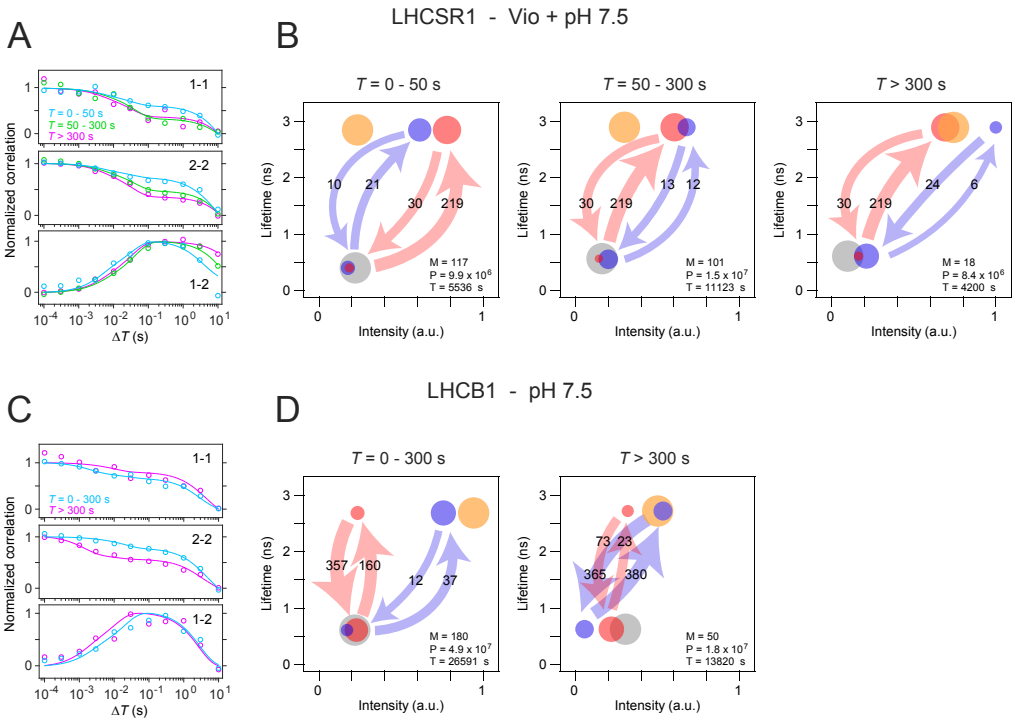

Figure S18: Correlation analysis at different time regions upon excitation. (***A***, ***C***) Correlation profiles estimated from the 2D-FLC analysis with the lifetime distribution set as a free fitting parameter in the time range of T = 0 - 50 (light blue), 50 - 300 (green), and > 300 s (pink) in LHCSR1 with Vio at pH 7.5 (***A***) and T = 0 - 300 (light blue) and > 300 s (pink) in LHCB1 at pH 7.5 (***C***). The obtained lifetime distributions are shown in Fig. S17. The solid line indicates a fitting correlation curve calculated based on three dynamic components as illustrated in ***B*** and ***D***, where the orange and gray circles correspond to active and quenched states, respectively, of the static component shown in gray in Fig. 3. The number on the arrow indicates the rate in 1/s. The total number of molecules (M) and photons (P) and the sum of measurement times (T) used in the analysis at each T region are also shown in the lower right of each diagram. In LHCSR1-V-7.5, dynamic properties of the active-biased component (red) were set to be constant except for the abundance ratio, and those of the other components were set as free fitting parameters. In LHCB1-7.5, on the other hand, at $T < 300$ s the parameters of the two dynamic components (red and blue) were fixed except for their abundance ratios, while at $T > 300$ s those of all three components were freely estimated.

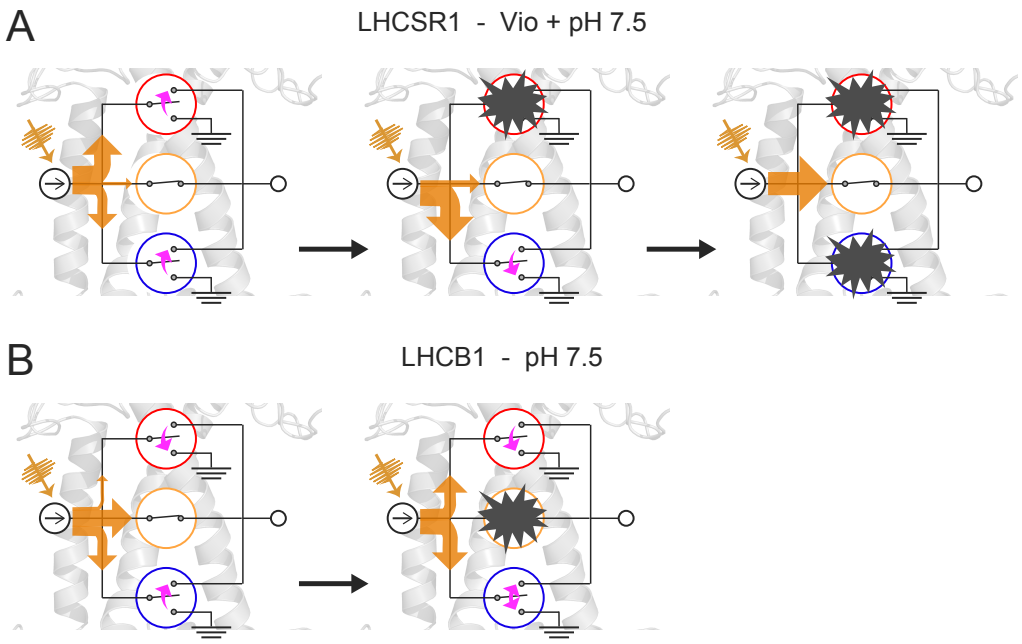

Figure S19: Stepwise photobleaching taking place at discrete NPQ sites. (***A***, ***B***) Schematic of the sequential photobleaching, leading to the photobleach-induced NPQ, in LHCSR1-V-7.5 (***A***) and LHCB1-7.5 (***B***). Three energy sinks emitting fluorescence photons are indicated by circles, the color of which corresponds to that of the dynamic component in Fig. S18*B* and *D*. The switching dynamics between active and quenched states, corresponding to on and off states, respectively, is indicated by a pink arrow, which points to a more stable state or is double-headed when balanced between the two states. The stepwise photodamages of energy emitter along with black arrows induce the changeover of energy flow as described by orange arrows, the thickness of which reflects the amount of light energy transported to each terminal energy sink. In natural membrane system, where the supercomplex is composed of RC and various LHCs, the output energy is transferred to adjacent LHCs through energy sinks.

1. Ishii K, Tahara T (2013) Two-dimensional fluorescence lifetime correlation spectroscopy. 2. Application. *J Phys Chem B* 117:11423–11432.
2. Ishii K, Tahara T (2012) Extracting decay curves of the correlated fluorescence photons measured in fluorescence correlation spectroscopy. *Chem Phys Lett* 519:130–133.
3. Ishii K, Tahara T (2013) Two-dimensional fluorescence lifetime correlation spectroscopy. 1. Principle. *J Phys Chem B* 117:11414–11422.
4. Elson EL, Magde D (1974) Fluorescence correlation spectroscopy. I. Conceptual basis and theory. *Biopolymers* 13:1–27.
5. Wentworth M, Ruban AV, Horton P (2003) Thermodynamic investigation into the mechanism of the chlorophyll fluorescence quenching in isolated photosystem II light-harvesting complexes. *J Biol Chem* 278:21845–21850.
6. van Oort B, van Hoek A, Ruban AV, van Amerongen H (2007) Equilibrium between quenched and nonquenched conformations of the major plant light-harvesting complex studied with high-pressure time-resolved fluorescence. *J Phys Chem B* 111:7631–7637.
7. Liu Z, et al. (2004) Crystal structure of spinach major light-harvesting complex at 2.72 Å resolution. *Nature* 428:287–292.
8. Tokutsu R, Minagawa J (2013) Energy-dissipative supercomplex of photosystem II associated with LHCSR3 in *Chlamydomonas reinhardtii*. *Proc Natl Acad Sci USA* 110:10016–10021.
9. Pinnola A, et al. (2015) Light-harvesting complex stress-related proteins catalyze excess energy dissipation in both photosystems of *Physcomitrella patens*. *Plant Cell* 27:3213–3227.
10. Kosuge K, et al. (2018) LHCSR1-dependent fluorescence quenching is mediated by excitation energy transfer from LHCII to photosystem I in *Chlamydomonas reinhardtii*. *Proc Natl Acad Sci USA* 115:3722–3727.
11. Kondo T, et al. (2017) Single-molecule spectroscopy of LHCSR1 protein dynamics identifies two distinct states responsible for multi-timescale photosynthetic photoprotection. *Nat Chem* 9:772–778.
12. Iwai M, Yokono M, Inada N, Minagawa J (2010) Live-cell imaging of photosystem II antenna dissociation during state transitions. *Proc Natl Acad Sci USA* 107:2337–2342.
13. Aro E, et al. (2004) Dynamics of photosystem II: a proteomic approach to thylakoid protein complexes. *J Exp Bot* 56:347–356.
14. Rochaix JD (2014) Regulation and dynamics of the light-harvesting system. *Annu Rev Plant Biol* 65:287–309.
15. Schuenemann D, et al. (1998) A novel signal recognition particle targets light-harvesting proteins to the thylakoid membranes. *Proc Natl Acad Sci USA* 95:10312–10316.
16. Pospíšil P (2012) Molecular mechanisms of production and scavenging of reactive oxygen species by photosystem II. *Biochim Biophys Acta* 1817:218–231.
17. Pinnola A, Bassi R (2018) Molecular mechanisms involved in plant photoprotection. *Biochem Soc Trans* 46:467–482.
18. Peers G, et al. (2009) An ancient light-harvesting protein is critical for the regulation of algal photosynthesis. *Nature* 462:518–521.
19. Alboresi A, Gerotto C, Giacometti GM, Bassi R, Morosinotto T (2010) *Physcomitrella patens* mutants affected on heat dissipation clarify the evolution of photoprotection mechanisms upon land colonization. *Proc Natl Acad Sci USA* 107:11128–11133.
20. Morosinotto T, Bassi R (2014) Molecular mechanisms for activation of non-photochemical fluorescence quenching: from unicellular algae to mosses and higher plants in *Non-Photochemical Quenching and Energy Dissipation in Plants, Algae and Cyanobacteria*. (Springer), pp. 315–331.
21. Pinnola A, et al. (2015) Heterologous expression of moss light-harvesting complex stress-related 1 (LHCSR1), the chlorophyll *a*-xanthophyll pigment-protein complex catalyzing non-photochemical quenching, in *Nicotiana* sp. *J Biol Chem* 290:24340–24354.
22. Remelli R, Varotto C, Sandonà D, Croce R, Bassi R (1999) Chlorophyll binding to monomeric light-harvesting complex; A mutation analysis of chromophore-binding residues. *J Biol Chem* 274:33510–33521.
23. Aitken CE, Marshall RA, Puglisi JD (2008) An oxygen scavenging system for improvement of dye stability in single-molecule fluorescence experiments. *Biophys J* 94:1826–1835.
24. Swoboda M, et al. (2012) Enzymatic oxygen scavenging for photostability without pH drop in single-molecule experiments. *ACS Nano* 6:6364–6369.
25. Peterman E, Dukker FM, Van Grondelle R, Van Amerongen H (1995) Chlorophyll *a* and carotenoid triplet states in light-harvesting complex II of higher plants. *Biophys J* 69:2670–2678.
26. Schödel R, Irrgang KD, Voigt J, Renger G (1999) Quenching of chlorophyll fluorescence by triplets in solubilized light-harvesting complex II (LHCII). *Biophys J* 76:2238–2248.
27. Gruber JM, Chmeliov J, Krüger TP, Valkunas L, Van Grondelle R (2015) Singlet–triplet annihilation in single LHCII complexes. *Phys Chem Chem Phys* 17:19844–19853.
28. Schlau-Cohen GS, et al. (2009) Pathways of energy flow in LHCII from two-dimensional electronic spectroscopy. *J Phys Chem B* 113:15352–15363.
29. Novoderezhkin V, Marin A, van Grondelle R (2011) Intra- and inter-monomeric transfers in the light harvesting LHCII complex: the redfield–förster picture. *Phys Chem Chem Phys* 13:17093–17103.
30. Rutkauskas D, Novoderezkhin V, Cogdell RJ, van Grondelle R (2004) Fluorescence spectral fluctuations of single LH2 complexes from *Rhodopseudomonas acidophila* strain 10050. *Biochemistry* 43:4431–4438.